

Status and application of advanced airborne hyperspectral imaging technology: A review

Jianxin Jia, Yueming Wang, Jinsong Chen, Ran Guo, Rong Shu, Jianyu Wang

PII: S1350-4495(19)30764-9

DOI: <https://doi.org/10.1016/j.infrared.2019.103115>

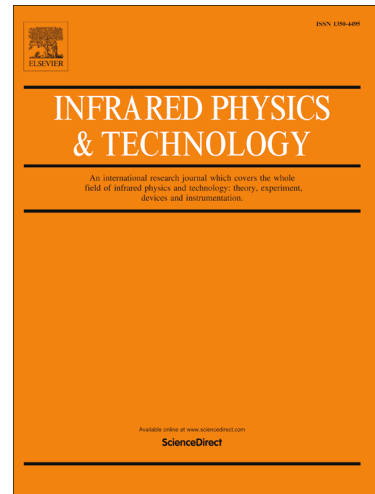
Reference: INFPHY 103115

To appear in: *Infrared Physics & Technology*

Received Date: 18 September 2019

Revised Date: 12 October 2019

Accepted Date: 6 November 2019



Please cite this article as: J. Jia, Y. Wang, J. Chen, R. Guo, R. Shu, J. Wang, Status and application of advanced airborne hyperspectral imaging technology: A review, *Infrared Physics & Technology* (2019), doi: <https://doi.org/10.1016/j.infrared.2019.103115>

This is a PDF file of an article that has undergone enhancements after acceptance, such as the addition of a cover page and metadata, and formatting for readability, but it is not yet the definitive version of record. This version will undergo additional copyediting, typesetting and review before it is published in its final form, but we are providing this version to give early visibility of the article. Please note that, during the production process, errors may be discovered which could affect the content, and all legal disclaimers that apply to the journal pertain.

Status and application of advanced airborne hyperspectral imaging technology: a review

Jianxin Jia^{a,b,c}, Yueming Wang^{a*}, Jinsong Chen^{b,c}, Ran Guo^{a,d}, Rong Shu^a, Jianyu Wang^a

- a. Key Laboratory of Space Active Opto-Electronics Technology, Shanghai Institute of Technical Physics, Chinese Academy of Sciences, Shanghai, 200083, China
- b. Center for Geo-Spatial Information, Shenzhen Institutes of Advanced Technology, Chinese Academy of Sciences, Shenzhen, 518055, China
- c. Shenzhen Engineering Laboratory of Ocean Environmental Big Data Analysis and Application, Shenzhen, 518055, China
- d. University of Chinese Academy of Sciences, Beijing, 100049, China

*Email: wangym@mail.sitp.ac.cn

Hyperspectral imaging technology has evolved for over thirty years and is widely used for geologic mapping, environmental monitoring, vegetation analysis, atmospheric characterization, biological and chemical detection, etc. With advances in technology, hyperspectral imagery not only determines the presence of materials and objects, but more importantly, also quantifies the variability and abundance of the identified materials or objects. Airborne hyperspectral imagers still perform a vital role in remote sensing fields due to advantages of spatial resolution, performance capabilities in a cloudy atmosphere, and onboard maintenance as compared to similar imagers aboard spaceborne platforms. To date, hundreds of airborne hyperspectral systems have been designed, built, and operated. Here, a review of key technologies for airborne hyperspectral imaging technology during past three decades is presented. First discussed will be high data rate imaging modes, high quality spectroscopic subsystems, and high sensitivity detector technology used on current airborne hyperspectral imagers. Particularly, the importance of data-processing such as calibration, geometric rectification, and atmospheric correction are discussed. Next, several new and novel applications are presented on the basis of state-of-the-art airborne hyperspectral technology. Finally, an outlook of challenges and future technology directions is presented along with general advice for designing and realizing novel high-performance airborne hyperspectral systems in this rapidly evolving field. By illustrating the status and prospects of typical airborne hyperspectral imagers, this overview provides a comparison of the technologies employed in previous hyperspectral imaging systems, current imaging technology research programs and prospects for innovative technology in future airborne hyperspectral imaging platforms.

Key words: airborne, hyperspectral, key technology, surface reflectance, application

1 Introduction

In the past thirty years, hyperspectral imaging technology has been widely used for geologic mapping, environmental monitoring, vegetation analysis, atmospheric characterization, biological and chemical detection, and disaster assessment [1–13]. It is important for many military applications, such as defeating camouflage, gathering information about battlespace, discrimination between targets and decoys, detection of weapons of mass destruction, and monitoring of international treaty compliance [14–21]. Airborne hyperspectral imagers still perform a vital role in remote sensing due to advantages of spatial resolution, performance capabilities in a cloudy atmosphere, as compared to similar imagers on spaceborne platforms [22–24]. Typical airborne hyperspectral systems such as; the Airborne Imaging Spectrometer (AIS) [25], Airborne Hyperspectral Scanner (AHS) [26], Airborne Imaging Spectrometer

for different Applications (AISA) [27], Airborne Prism Experiment (APEX) [28], Airborne Reflective Emissive Spectrometer (ARES) [29], Visible/Near-Infrared Imaging Spectrometer (AVIRIS) [30], Digital Airborne Imaging Spectrometer (DAIS-7915) [31], Hyperspectral Mapper (HyMap) [32], Hyperspectral Digital Imagery Collection Experiment (HYDICE) [33], Multispectral Infrared and Visible Imaging Spectrometer (MIVIS) [34], and the Operational Modular Imaging Spectrometer (OMIS) [35] were developed before the year 2000. Since that time performance of hyperspectral instruments has improved greatly thus expanding their applications. Since 2010, the technologies of restricted bandwidth sensors such as those employed by the Compact Airborne Spectrographic Imager (CASI) / Short-wave-infrared Airborne Spectrographic Imager (SASI) / Thermal-infrared Airborne Spectrographic Imager (TASI) [36] were applied to new integrated airborne hyperspectral imagers, such as Next Generation Visible/Near-Infrared Imaging Spectrometer (AVIRIS-NG) [37], Full spectrum Airborne Hyperspectral Imager (FAHI) [38], Hyperspectral Thermal Emission Spectrometer (HyTES) [39,40], and SYSIPHE [21]. Several operational parameters currently in use are shown in Table 1.

Table 1 Summary of typical airborne hyperspectral imagers

Name	Developer	Spectral range (μm)	Number of bands	Spectral sampling interval (nm)	IFOV (mrad)	FOV (°)
AISA-FENIX 1K [41]	Specim, Finland	0.38–0.97, 0.97–2.5	348, 246	≤4.5, ≤12	0.68	40
APEX [28]	ESA, Switzerland, Belgian	0.372–1.015 0.94–2.54	114, 198	0.45–0.75, 5–10	0.489	28.1
AVIRIS-NG [37,42]	NASA/JPL, USA	0.38–2.52	430	5	1	34
CASI-1500 [43]/ SASI-1000A [44]/ TASI-600 [45]	Itres, Canada	0.38–1.05, 0.95–2.45, 8–11.5 0.4–0.95,	288, 100, 32 256,	2.3, 15, 110 2.34,	0.49, 1.22, 1.19 0.25,	40
FAHI [38]	China	0.95–2.5, 8–12.5 0.4–1,	512, 128 5	3, 32 5,	0.5, 1 0.25	40
SYSIPHE [21]	France and Norway	0.95–2.5, 3–5.4, 8.1–11.8	560 (total)	6.1, 11 cm^{-1} , 5 cm^{-1}	0.25	15

Hyperspectral image data information can be divided into six levels as a function of improvement in spectral resolution and instrument performance. Level 1: detection; determines the presence of materials, objects, activities, or events. Level 2: classification; separates materials into spectrally similar groups. Level 3: discrimination; determines generic categories of the previous classes. Level 4: identification; determines the unique identity of the previous categories. Level 5: characterization; determines variability of identified material (e.g. wet/dry sand, soil particle size effects). Level 6: quantification; determines the abundance of materials [46–49]. In early technology employment hyperspectral imaging was mainly used for material detection and classification. With the improvement of material surface reflectance detection accuracy, the goal of characterization and quantification has been achieved in recent years. AVIRIS-NG has been successfully used to retrieve columnar density and sources of methane (CH_4)

due to such technology improvement. This instrument has achieved a mean reflectance accuracy of 1.0% on diverse validation surfaces and limited opto-thermal-mechanical distortions to less than 0.01 percent of a pixel. In addition, AVIRIS-NG has a signal to noise ratio (SNR) of 2000 in the visible to near-infrared (VNIR) spectral range and 1000 in the shortwave infrared (SWIR) region, respectively [50–52]. Kruse combined AVIRIS (0.4–2.5 μm) and HyTES (8–12 μm) data for geologic mapping, which brought out subtle associations for geologic mapping that are not easily observable by mapping the spectrally predominant material in individual ranges [53]. Another similar application is the CASI/SASI/TASI hyperspectral data that was combined to characterize the uranium mineralization of granite and sandstone-type uranium deposits in the south and northwest areas of China [36]. These new applications in recent years require higher instrument performance, not only for spatial and spectral resolution, but more importantly system stability and accuracy, which include the accuracy of radiometric calibration, geometric and atmosphere correction.

The goal of this paper is to describe the current evolutionary trends in airborne hyperspectral sensor development and to analyze the key technologies required to achieve the goal of characterization and quantification. Key technologies of typical airborne hyperspectral systems are described in detail in Section 2. Section 3 presents some new applications and variations in recent years with the evolution of airborne hyperspectral technology. A comparison of the technologies employed in previous hyperspectral imaging systems, current imaging technology research programs and prospects for innovative technology in future airborne hyperspectral imaging platforms is presented in Section 4. Conclusions are presented in Section 5.

2 Key technologies

Instrument performance and data pre-processing results are among factors necessary for the acquisition of high accuracy surface reflectance data. Field of view (FOV), spectral range, spatial resolution, spectral resolution, and sensitivity are high level specifications of instrument performance. Data pre-processing consists of calibration, geometric rectification, and atmospheric correction. The hyperspectral imager is a complex system. Other key imager technologies include; a high data throughout imaging mode, a high-quality spectroscopic subsystem, a high sensitivity detector and a high stability thermally controlled environment. We have focused on the imaging mode, spectroscopic subsystem, detector technology and data pre-processing technologies in this paper.

As with all complex data processing systems, there are trade-offs for instrument specifications when designing an airborne hyperspectral imaging system. Reducing the pixel size of the detector can increase the spatial resolution but will reduce the effective detection energy collected by optics. Precision spectral resolution will also reduce the effective detection energy of each spectral band of the imaging spectrometer. Increasing the aperture of the optical system will increase the effective detection energy entering the instrument, but this will inevitably lead to an increase in volume and weight [54]. It can be seen from Eq.1 and 2, that the signal to noise ratio (SNR) is limited by the aperture, detector pixel size, instantaneous field of view (IFOV), and integration time [55]. To improve the SNR requires an increase in both the aperture and IFOV, but it also will also increase the cost and system complexity of the instrument and decrease the spatial resolution simultaneously. The spectral resolution definition needs to be consistent with the instrument sensitivity; the higher the spectral resolution, the lower the energy in each spectral band and the worse SNR. Therefore, it is necessary to balance spatial resolution, spectral resolution, time resolution, sensitivity and instrument volume and weight to ensure the design performance of the instrument for airborne hyperspectral imager.

$$SNR = \frac{D_0^2 \beta^2 T_{int} \sin \theta}{4hcN_{noise}} \int_{\lambda_1}^{\lambda_2} E(\lambda) \tau_o(\lambda) \tau_a(\lambda) \rho(\lambda) \eta(\lambda) \lambda d\lambda \quad (1)$$

For $\beta = d/f$, $F\# = f/D_0$, Eq. 1 can be written as:

$$SNR = \frac{d^2 T_{int} \sin \theta}{4(F\#)^2 hcN_{noise}} \int_{\lambda_1}^{\lambda_2} E(\lambda) \tau_o(\lambda) \tau_a(\lambda) \rho(\lambda) \eta(\lambda) \lambda d\lambda \quad (2)$$

Where D_0 is the optical effective aperture diameter, d is the detector pixel size, β is the IFOV, T_{int} is the detector integration time, θ represents the sun elevation angle, h represents Planck's constant, c is the velocity of light, N_{noise} is the sum of various noise electrons number, $F\#$ is the system F number, λ represents the wavelength, $E(\lambda)$ represents the solar spectral irradiance at the ground surface, $\tau_o(\lambda)$ is the total spectral transmittance of the optical system, $\tau_a(\lambda)$ is the spectral transmittance of the atmosphere, $\rho(\lambda)$ is the surface albedo, $\eta(\lambda)$ is the detector quantum efficiency.

2.1 Imaging mode

Unlike the general two-dimensional image, hyperspectral image data is three dimensional (two spatial and one spectral). Commonly, scanning in the spatial dimension is along the direction of the platform motion using a two-dimensional detector or focal plane array (FPA) and can be mainly divided into either whiskbroom and pushbroom terminology by scanning mode, as shown in Fig. 1.

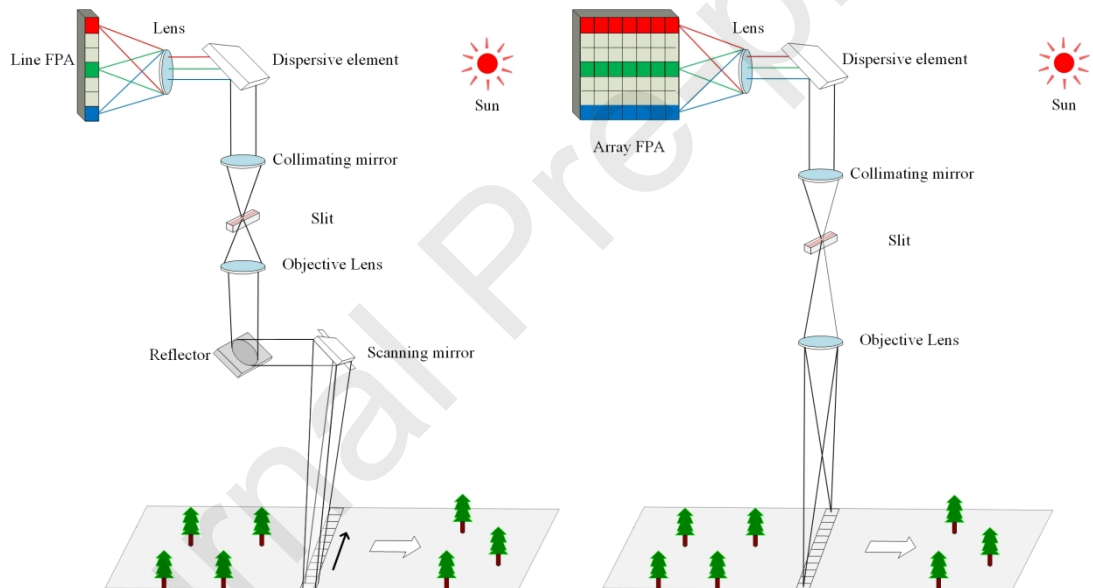


Fig. 1 Whiskbroom and pushbroom imaging mode. (a) Whiskbroom. (b) Pushbroom.

Whiskbroom is a common imaging mode for early airborne hyperspectral imagers, such as AHS, ARES, AVIRIS, DAIS-7915, MIVIS, OMIS, and HyMap. The scanning mirror is swept from one endpoint of the swath width to the other endpoint to complete the spatial dimension imaging in across-track direction, while the motion of the platform completes the spatial dimension imaging in the along-track direction. Imaging in the spectral dimension is performed by the spectroscopic system and the line array detector. The advantage of the whiskbroom hyperspectral imager is that it can achieve a larger FOV e.g. HyMap FOV is up to 70 degrees, but the SNR is always lower than pushbroom instrument because of shorter pixel light integration dwell time.

With the development of semiconductor technology, large area focal plane arrays (FPA) can be used in airborne hyperspectral imagers. In this application the pushbroom imaging mode was utilized such as in instruments including; AIS, AISA, APEX, AVIRIS-NG, CASI, FAHI, HYDICE, HyTES, and

SYSIPHE, etc. Compared with a whiskbroom hyperspectral imager, the main difference to a pushbroom scanning system is that there is no complex mechanical scanning mechanism and the pixel dwell time is increased. Due to the lack of a mechanical scanning mechanism, the pushbroom instrument weight and volume are lower and the SNR can be significantly improved. For example, the SNR of AVIRIS is improved from 150 to 2000 mainly by changing the whiskbroom imaging mode to pushbroom [51,56]. However, a disadvantage of a pushbroom hyperspectral imager is that it is very difficult to balance a large FOV with a small IFOV. Some new technologies are used to enlarge the FOV, such as FAHI using three modules to achieve a 40 degree FOV [57]. In addition, the development of detector technology can also compensate for this drawback.

The step-stare imaging mode, which is less frequently applied to airborne hyperspectral systems, uses an array detector with a sufficient number of pixels to simultaneously acquire the two spatial dimensions of the data cube and the spectral information in a time interval. Compared with the scanning imaging spectrometer, the main difference is that the speed of the aircraft determines the dwell time for each pixel in the scanning systems, while for the step-stare system the dwell time is not controlled by the speed of the aircraft. The drawback is that more complicated post-processing is needed to obtain the information from the different spectral bands of energy reflected from the target. The step-stare imaging spectrometer is generally used for close-range detection, such as the spaceborne VNIR imaging spectrometer in the Chang'e-3 of China [58,59].

2.2 Spectroscopic subsystem

A spectroscopic subsystem, which determines the spectral performance, mechanism complexity, weight, and volume, is the key part of a hyperspectral imager. There are many different types of spectrometers for spectral division that are suitable for different applications. They can be divided into three main classes: dispersive spectrometer, Fourier transform interferometer (FTI), and filter spectrometer. The dispersive spectrometer is the spectroscopic technology that was first applied to spectral imaging instruments and has been deployed both on airborne and spaceborne platforms for many years. To date, most mainstream airborne hyperspectral imagers use a dispersive spectrometer, which itself can be divided into grating and prism type spectrographs according to the adopted dispersive element, as shown in Fig. 2. A typical prism or grating imaging spectrometer has optics to focus the incident radiation on a slit, collimating optics to bring parallel rays to the dispersing element and focusing optics to focus the dispersed radiation on the detector array. Each detector pixel in the array acts as the exit slit. High accuracy matching of the detector size and the entrance slit is necessary for optimum performance. By coupling the dispersing grating or prism with a lens and a two-dimensional array of detectors, a spectral image is formed where the spatial information is along one axis and spectral information is along with the other [60].

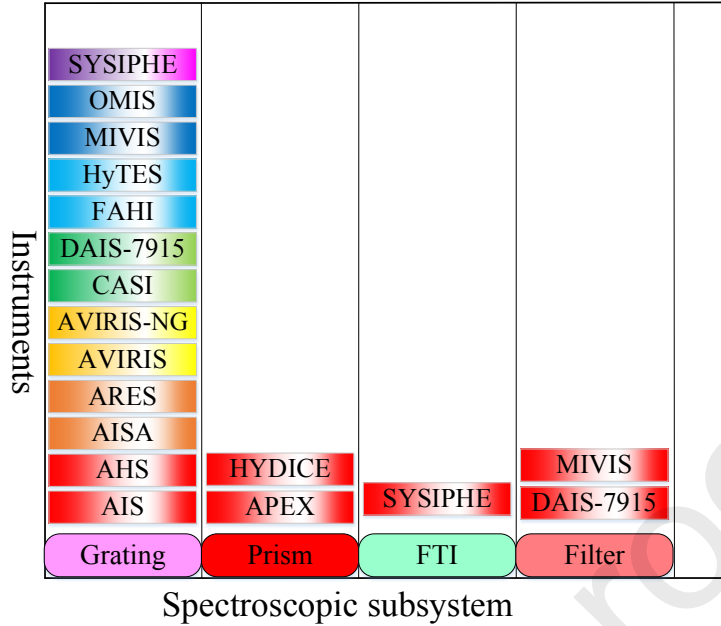


Fig. 2 Spectroscopic subsystems of some typical airborne hyperspectral imagers.

The prism spectrometer mainly utilizes the dispersion principle of the prism. Monochromatic light is deflected after being refracted by the wedge and the different wavelengths produce different deflection angles to achieve the spectroscopic requirement. Generally, a prism spectrometer has the advantages of uniformly high optical efficiency, wide spectral response characteristics, and low scattering [61]. Hyperspectral imagers that use this spectroscopic technology include APEX and HYDICE. However, the dispersion is nonlinear after the different wavelengths of light pass through the prism, thereby the spatial position and separation between the different wavelength bands are seriously unbalanced.

Grating spectrometers utilize the principle of optical diffraction and are mainly divided into two types: transmissive grating and reflective grating. The basic transmission diffraction grating consists of a large number of small slits equally sized and spaced. Each single slit causes a diffraction fringe, and light waves from the respective slits create interference patterns. Thus, a combined interference-diffraction fringe is formed at the focal plane of the lens, and the maximum position of the fringes is related to the wavelength, thereby obtaining the dispersion line we need. Generally, the maximum energy of the grating optical signal is in the "zero-order" position of the dispersion, and the spectral distribution of the specific position can be realized by the planar blazed grating. As the dispersive component of the imaging spectrometer, the grating has the greatest advantage in that the spectral dispersion is linear. The wavelength position of the maximum diffracted energy can be adjusted by changing the blaze angle and is used in the full spectrum band. Most popular airborne hyperspectral imagers use grating spectroscopic technology, as shown in Fig. 2.

Fourier transform interference spectrometers can be divided into either dynamic time modulation or static space modulation types. A Michelson interferometer is a typical temporal modulation spectrometer where the core of the time-modulated Fourier imaging spectrometer is a Michelson interferometer. The intensity of the incoming light is modulated by the path difference from the motion of the moving mirror to form an interference image. The interference image is recorded, and the spectral image of the target point can be obtained by Fourier transform.

The spatial modulation Fourier imaging spectrometer generates the light path difference by a light beam splitter and a reflecting mirror to pass a beam of light from the ground, and spatially coherent interference fringes can be obtained on the image plane. The interference image is also recorded, and the spectral image of the target is acquired by Fourier transform inversion. Compared with other spectrometers, the advantage of the Fourier imaging spectrometer is high luminous flux, which leads to higher SNR and spectral resolution at the same time. But the major limitations are that the Fourier imaging spectrometer needs a complex opto-mechanical structure and a high platform stability. Medium wave infrared (MWIR) and LWIR imaging spectrometers of the SYSIPHE system are composed of a static Fourier Transform Spectrometer, based on a modified Michelson interferometer, placed in front of the imaging optics, as shown in Fig. 3 [20]. The two main parts are the Michelson interferometer and the downstream imaging optics. The light coming from the ground scene first enters the instrument through a wide-band window, which encloses the cryostat in which the optics are integrated. The bending mirror rotates the rays by 90° to make them be incident with an angle of 45° on the beam splitter inside the interferometer. The light then follows a path through the interferometer, propagates into the imaging optics and is finally focused on the optics focal plane. The mirrors of the interferometer are set so that the maximum optical path difference is about 467 μm in the MWIR and 993 μm in the LWIR, to reach the expected spectral resolution [20].

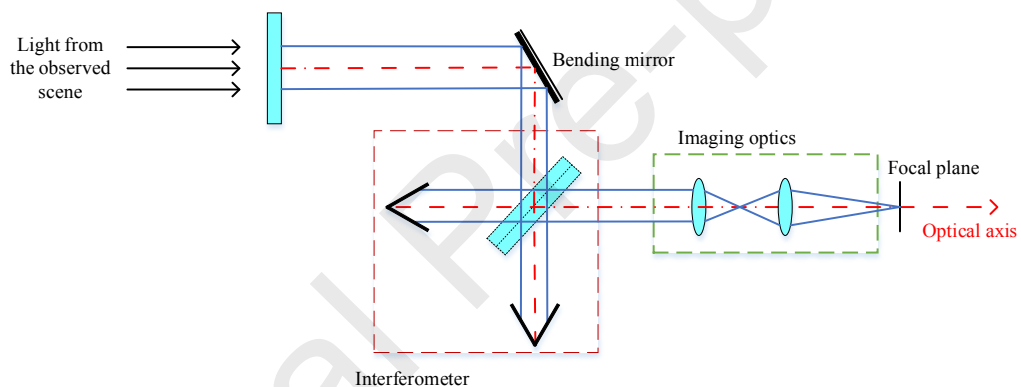


Fig. 3 Optical architecture of the SYSIPHE MWIR and LWIR imaging spectrometers.

It is worth noting that besides designing the optics to be fast and with high resolution, it is also important to minimize distortions, such as smile and keystone. Many technologies have been used in airborne hyperspectral imagers to decrease the smile and keystone effects and have achieved good results. The smile and keystone of AISA-FENIX are less than 0.2 pixels, AISA-FENIX 1K are less than 0.35 pixels [62]. The smile of APEX is less than 0.16 pixel for 90% of all pixels and 0.35 pixel for 10% of all pixels, the keystone of APEX is less than 0.16 pixel for 80% of all pixels and 0.35 pixel for 20% of all pixels [28]. The smile and keystone of SYSIPHE VNIR and SWIR spectrometers are less than 0.1 pixels [63].

A filter imaging spectrometer contains a rotating filter, wedge filter, acousto-optical tunable filter (AOTF), and liquid crystal tunable filter (LCTF). AOTF was used in the spaceborne VNIR imaging spectrometer in the Chang'e-3 of China [58,59].

2.3 Detector technology

The detector is an important element for a hyperspectral imaging system and is used with an adapted spectral response to fit the waveband of the instrument. It can be seen from Eq.1 and 2, that the detector, optical system, and instrument sensitivity are interrelated. Therefore, the detector selection should

consider the instrument volume, weight, and SNR to in order to meet the system performance requirements. For airborne hyperspectral applications, several physical parameters are relevant; quantum efficiency describes the ability of the detector to convert photons to electronic charges for a given pixel; modulation transfer function (MTF) corresponds to the response of the detector in the spatial frequency space; thermal electron dark current generated by the photodiodes can lead to a degradation of the SNR ratio, and therefore needs to be minimized; and frame rate needs to match the aircraft speed [64].

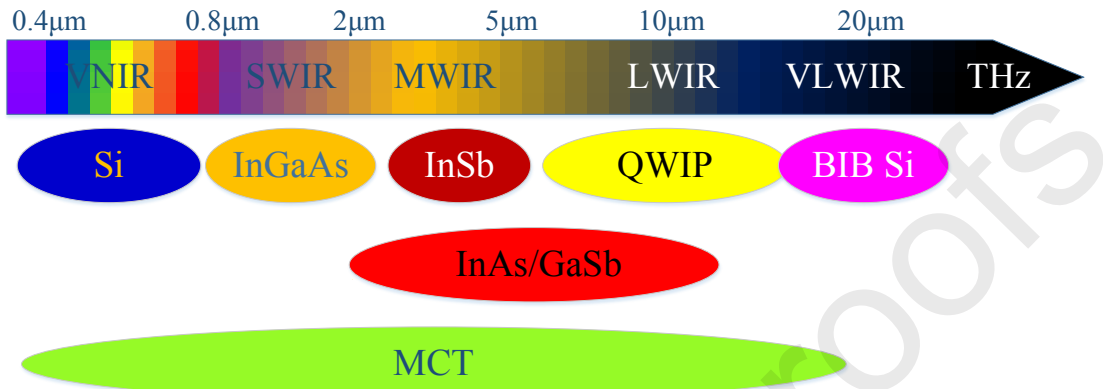


Fig. 4 Detection technologies covering the infrared spectrum.

Various materials have been used for the detector according to their spectral response range, as shown in Fig. 4 [64]. Thanks to the ability of mercury cadmium telluride (MCT or HgCdTe) material to be tuned in terms of cut-off wavelength (via the Cd/Hg ratio of the $\text{Cd}_x\text{Hg}_{1-x}\text{Te}$ alloy), it is possible to cover a very wide detection bandwidth from 0.4 μm up to nearly 20 μm [65–68]. Thus, most of the infrared spectrum can be covered with only one type of material, contrary to most of the other detector materials used for infrared detection, which makes MCT a material of choice in that field [69,70]. The main detector manufacturers include American companies Rockwell International Science Center, Raytheon, Teledyne (which acquired British E2V in 2016), Sensors Unlimited, and France's Sofradir [71]. The HgCdTe detector array of AVIRIS-NG was built by Teledyne Imaging Sensors Inc. [72], the APEX VNIR CCD detector made by E2V [73] and the SWIR MCT detector made by Sofradir [28], SYSIPHE MWIR and LWIR detectors also were provided by Sofradir [64]. In recent years, InAs/GaSb Type-II superlattices have proven to be an excellent material for high end infrared detectors and are now competing with the traditional state-of-the-art technologies. Good detector performance has been demonstrated for single pixel detectors as well as for FPAs [74–77].

2.4 Calibration

Calibration, which encompasses spectral calibration and radiometric calibration, is very important for many remote sensing instruments, so does the airborne hyperspectral imager [78,79]. The requirement for spectral calibration derives from the need to accurately determine the wavelength ranges, the band center wavelengths, spectral resolution (full width at half maximum), and spectral sampling interval. Additionally, spectral calibration can be used to verify that the sensor has met specifications with regard to out of band leakage that could have been caused by problems such as scattered light or multi-order diffraction [80]. Radiometric calibration includes relative calibration and absolute calibration. The requirement for relative radiometric calibration, is defined as the spectral band-to-band calibration required to remove the effects of the non-uniformity of the detector response. The absolute radiometric calibration is used to convert the detector response digital number (DN) values to radiance received by the optical aperture. Both spectral and radiometric accuracy determine the results of airborne hyperspectral imager quantitative applications [81].

A monochromator, uniform light source, and collimator are commonly used for spectral calibration in the laboratory. The spectral response curves of each pixel are always fitted to a Gaussian curve [57,82,83]. The main factors that affect the spectral calibration accuracy are the monochromator accuracy, deviation of the response curve fitting, and variation in the angular uniformity of the collimator beam. With advances in instrument stability and monochromator accuracy, spectral calibration accuracy is increasing as well. The spectral calibration accuracy of the primitive AVIRIS instrument was improved from 2.1 nm to 1nm through several engineering and maintenance cycles. Main improvements were that the fiber optic spectrometer connector was improved to increase the repeatability and stability of the spectral alignment, a new automated spectral calibration capability was implemented, and an inflight spectral source was used to fully monitor the inflight spectral calibration of AVIRIS [84]. Currently, the spectral calibration accuracy of the airborne hyperspectral imager is better than 1 nm, and, as such, the accuracy of AVIRIS-NG is improved to 0.1nm [51], FAHI is 0.1nm [57] , SASI-1000A is 0.1 nm [44], and APEX is 0.2 nm [85].

To remove the effect of the non-uniformity of the detector response, such as blind pixel removal, destriping or noise processing, relative radiometric calibration is performed as the first step of the radiometric calibration procedure [86,87]. Exact relative radiometric calibration coefficients of sensors can be obtained through a calibration experiment, and then the images are corrected [88]. However, because of the problems of stray light interference, slit contamination, and instrument instability, hyperspectral images always remain affected by spatial dimension nonuniformity which appears as stripe noise after relative radiometric calibration. Therefore, many kinds of stripe noise processing methods are featured in the remote sensing literature, such as filtering [89–91], statistics [92,93], radiometric equalization [94], and subspace techniques [95–97]. Fig. 5 shows the correction results for FAHI using a new technique combining image statistics and spatial filtering algorithms [38].

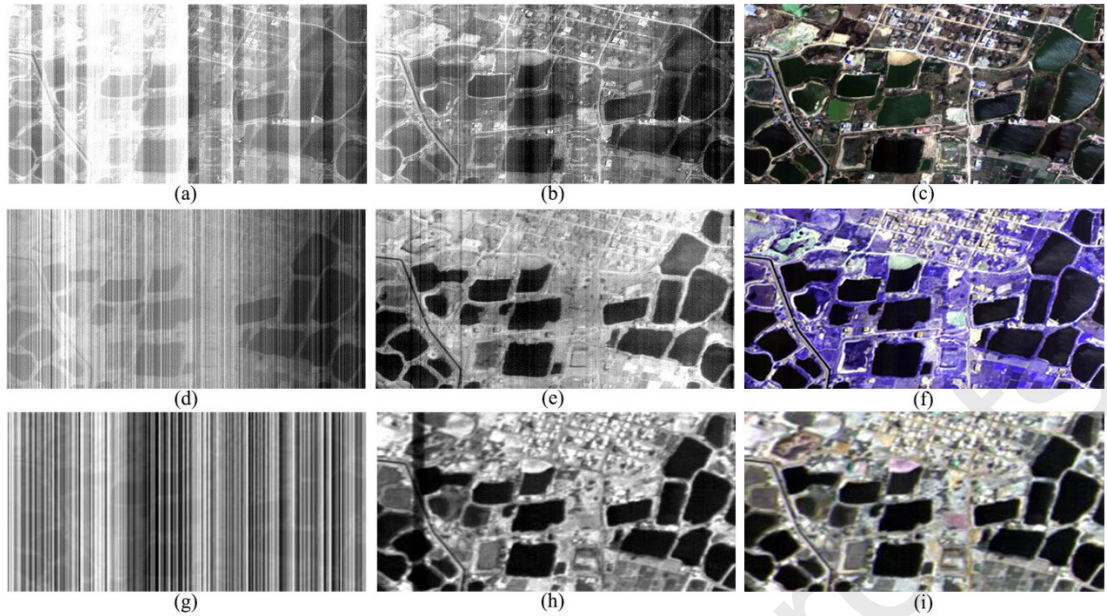


Fig. 5 The relative radiometric correction results of FAHI using laboratory calibration and destriping methods. (a) VNIR original image. (b) VNIR image corrected by laboratory calibration. (c) VNIR color image corrected by laboratory calibration and followed by destriping methods. (d) SWIR original image. (e) SWIR image corrected by laboratory calibration. (f) SWIR color image corrected by laboratory calibration and followed by destriping methods. (g) LWIR original image. (h) LWIR image corrected by laboratory calibration. (i) LWIR color image corrected by laboratory calibration and followed by destriping methods.

The image after relative radiometric correction can be used as a general two-dimensional image but cannot be applied to the quantitative application without absolute radiometric calibration.

High precision, stability standard radiance light sources are used to measure the relationship between the input spectral radiance and output DN value of each detector pixel to achieve absolute radiometric calibration of the airborne hyperspectral imager. An integrating sphere in the laboratory is always used in this procedure. There are many mathematical models for the input-output relationship of the system established by using the calibration data. The simplest and most commonly used include; a linear model, piecewise linear model, polynomial model, and various nonlinear models. With the evolution of detector and electronic technology, system linearity is improving over time. Therefore, many instruments are well described by a simple linear model. In addition, onboard calibration is also a commonly used method for airborne hyperspectral imagers, especially for thermal infrared detectors, which are greatly affected by the operating mode and ambient temperature. Usually, a high precision blackbody is used as the calibration source. The radiometric calibration accuracy is limited by the accuracy of the calibration instrument, the deviation of the mathematical model, the temporal stability of the imaging system, the spectral calibration of the imaging system, and such factors as sensitivity to polarization and to spectral and spatial stray light. With the progress of technology, the absolute radiometric calibration accuracy of airborne hyperspectral imagers has improved greatly. The absolute radiometric calibration accuracy of AVIRIS in 1987 is 10% [98] and was improved to 6% by replacing the onboard calibrator, improving calibrator stability, and using ground ancillary data [99]. The calibration accuracy for AVIRIS-NG is up to 5% and the linearity is better than 99% [51]. The accuracy of CASI is $\pm 2\%$ in 470–800 nm and $\pm 5\%$ in 430–870 nm range, respectively [100], and the result of CASI-1500 is better than 2% for full spectral

range [101]. The designed accuracy of APEX is less than 2%, but actually is 4.2% in VNIR and 6.6% in SWIR range, respectively [28].

Changes in external temperature, atmospheric pressure, color differences between a laboratory integrating sphere and sunlight drive the requirement for an in-flight calibration capability. Therefore, an important part of instrument characterization is resulting from the in-flight (onboard) calibration of instrument behavior over time [22]. Such in-situ calibration capability can monitor small spectral changes (spectral shift) using a broadband light source or other measurements mounted on the aircraft when the instrument is moved from a laboratory environment to an airborne setting [102]. Field radiometric calibration is achieved by deploying known targets on the ground, and is always used in conjunction with atmosphere correction data, as shown in Fig. 6 [21].

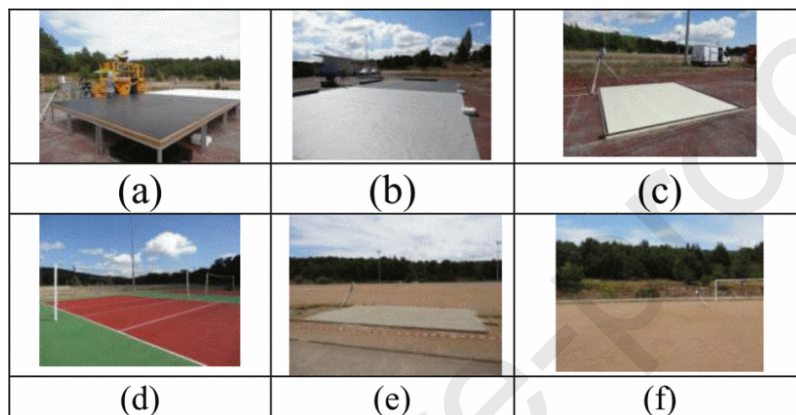


Fig. 6 Targets and reference ground surface for ground truth measurements. (a) Black and white panels, (b) Linoleum panels, (c) Polystyrene panel, (d) Painted concrete, (e) Sand, (f) Cay.

2.5 Geometric rectification

An airborne hyperspectral image is affected of geometric distortions due to instabilities in aircraft pitch, roll and yaw motions in flight and variations in altitude and/or ground speed during image acquisition. As shown in Fig. 7 [103], these distortions cause the image to be visually misinterpreted, which largely affects the traditional application of hyperspectral imagery. Therefore, geometric rectification is used to eliminate the geometric deformation of the image space and to make the object in the image match the actual geographical location. The image in Fig. 7 (b) is the result of geometric correction using position and orientation data. The distorted airport runway in Fig. 7 (a) has basically recovered its original appearance in the corrected image. The comparison before and after rectification proves the necessity of geometric correction of the airborne hyperspectral image.

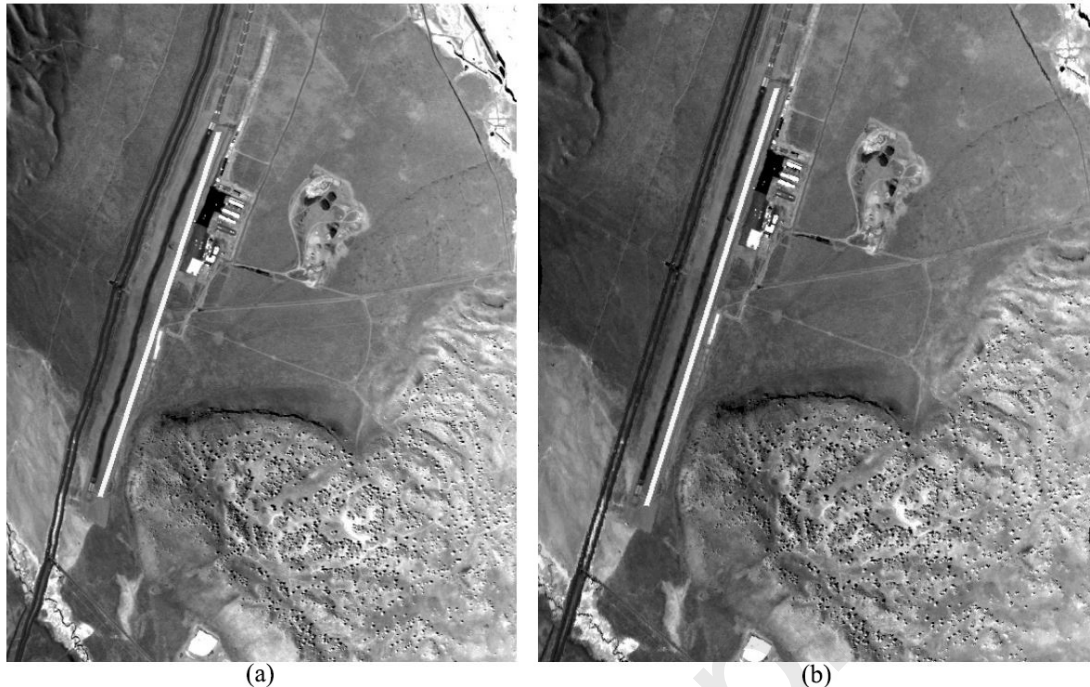


Fig. 7 (a) Raw HyMap image in the vicinity of the Mammoth Mountain airport. Note the curved runway (black line next to the drawn white reference line). (b) Results after geometric correction. Compare the straight runway to the reference line.

Geometric correction is achieved by resampling the distorted image to eliminate image distortion caused by aircraft pitch, roll and yaw according to a corresponding geometrical model which is based on the input of position and attitude data. Geometric correction can be divided into internal and external orientation element calibration. The calibration of the internal orientation element is mainly obtained by laboratory or external field calibration to obtain the main focus, main focal length, and distortion of the telescope system. The external orientation element of the instrument is obtained by the conversion of parameters such as the attitude and position of the aircraft platform. Subsequently, the geometric correction of the image is performed [104]. An inertial measurement unit (IMU) / Global Positioning System (GPS) combination system is mainly used for the position and attitude data acquisition to achieve improved accuracy and reduced cost. The IMU data contains all necessary information about the sensor position during the flight, i.e. roll, pitch, heading and yaw angles, the GPS provides coordinates of the flight track, altitude and time for every scanned image line [105]. A digital terrain elevation model (DTM) can be used for orthorectification by providing the terrain variation information. Several mature software packages have been applied to the geometric correction of airborne hyperspectral sensors and include; CaliGeo for the AISA [106], GeoCorr for the Iters sensors [107], and PARGE for HyMap, AVIRIS, and SYSIPHE [104]. Additionally, the imaging spectrometers are often mounted to a stabilized platform to ensure the instrument stability as soon as possible in aerial photogrammetric remote sensing, such as the PAV30 Gyro-stabilized platform using by APEX [108], PAV410 using by APEX [109], and PAV80 using by SYSIPHE [20] and FAHI. Fig. 8 shows some general geometric and radiometric correction components of CASI/SASI/TASI [36].

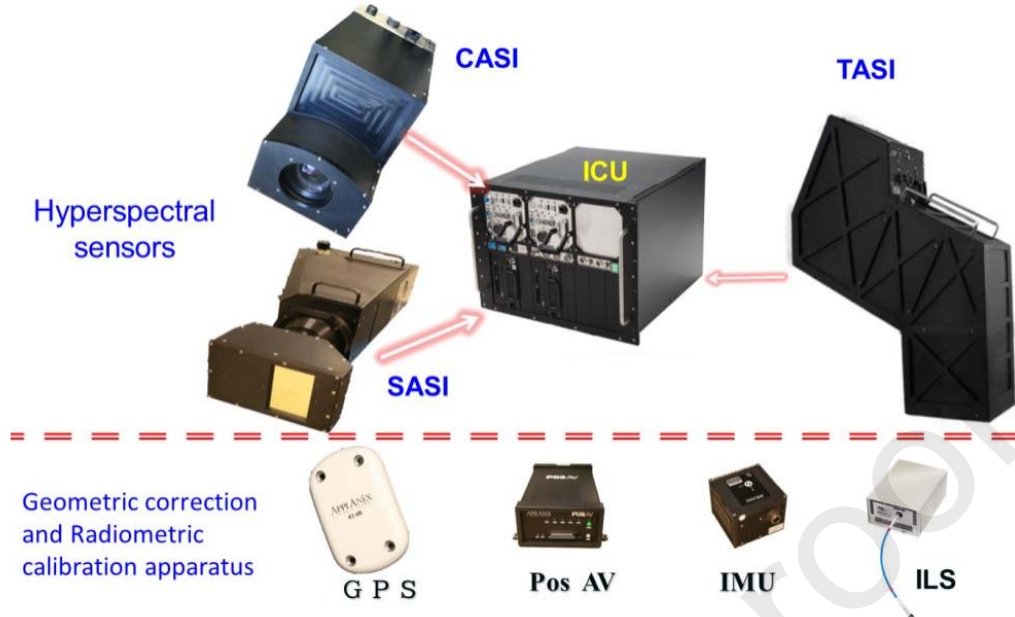


Fig. 8 Hyperspectral imaging system components of CASI/SASI/TASI.

The accuracy of the geometric correction is highly dependent on the given input data, especially the auxiliary navigation data and the accuracy of the flight path [105]. The geometric correction results of the mainstream hyperspectral imagers are improving using such external data sources as a vertical gyroscope and GPS data that were used for the geometric correction of the primitive CASI. With these data, a geometric grid accuracy of 3 to 5 pixels was obtained (about 30 meters on the ground), for the 17 points examined in detail. The major sources of error are likely terrain height variations and yaw error resulting from the lack of a heading gyro [100]. Accuracy was improved in later updated instruments by utilizing six orientation elements (three dimensional space and three axis attitude parameters provided by GPS/IMU) to recover the spatial feature of hyperspectral image [36]. A state-of-the-art GPS/INS “C-MIGITS II” system developed by Boeing was installed on HyMap starting with the 1999 flight season. The stated accuracy was 4.5 meters and 1 milliradian pointing accuracy when operated with differential GPS [103]. The accuracy was improved to 1.5 to 2 pixels by using IMU and DEM data [105].

2.6 Atmospheric correction

Hyperspectral imagery has good visibility and initial positioning after geometric correction, but still cannot be used quantitatively because of atmospheric effects caused by molecular and particulate scattering and absorption [110–112]. The task for earth observation is the mapping of surface properties. However, the surface information is masked, because the signal recorded by the airborne hyperspectral imager depends on the variety and quantity of several components during the radiation’s path from the sun to the ground and back to the sensor. Varying atmospheric conditions, differences in the sun geometry, and topographic effects strongly influence the recorded signal. These influences modify the true spectral behavior of the ground features. The objective of atmospheric correction is the elimination of atmospheric and illumination effects to convert the data from radiance to reflectance for the VNIR and SWIR spectrum range or emittance for the thermal infrared (TIR) spectrum range. This is necessary to retrieve the physical parameters of the surface. To carry out quantitative analysis and change detection applications with images from different periods of time and different sensors, accurate atmospheric correction is an essential part of pre-processing and a prerequisite for the derivation of products needed

for subsequent hyperspectral image processing and analysis steps [113].

Various atmospheric correction methods have been researched and applied during the past thirty years and can be divided into three main groups: (1) empirical models; (2) radiative transfer models; and (3) hybrid methods. Empirical models include empirical line (EL), internal average relative reflectance (IARR), Quick Atmospheric Correction (QUAC), and flat field calibration (FFC). These models assume that the image has a constant atmospheric effect and ignore the true atmospheric conditions during image acquisition and some additional effects like illumination direction, the topography of the represented surface or Bi-directional Reflection Factor (BRDF). The advantages of these methods are that they are simple and fast, but these advantages often come at a cost of reduced accuracy [114]. There are a series of software programs available to model the atmosphere including ATmospheric REMoval algorithm (ATREM), ATmospheric CORrection (ATCOR), Fast Line-of-sight Atmospheric Analysis of Spectral Hypercubes (FLAASH), High-accuracy ATmosphere Correction for Hyperspectral data (HATCH), and Atmospheric CORrection Now (ACORN), etc. These radiative transfer models, which use radiative transfer codes such as LOWTRAN, MODTRAN, 5S, and 6S, are based on physical approaches taking real atmospheric conditions into account. Hence, radiative transfer models generally are understood to be more accurate than empirical approaches and have become the standard for offline science data processing [115]. Hybrid methods include combinations of empirical approaches and radiative transfer models for the derivation of surface reflectance from hyperspectral imaging data. Each pre-processing technique includes its own assumptions. So there is a need to analyze the limitations of different pre-processing techniques and combine them with specific applications [116]. It is worth noting that the removal of the surface-reflected sky radiance should not be neglected, especially for ocean surface reflection [23].

As the atmospheric correction is important for hyperspectral data processing, the accuracy affects subsequent applications greatly. Instrument performance (uncertainties of calibration, SNR) and correction models are the main limitation factors for atmospheric correction accuracy. For example, one of the most important sources of error in atmospheric correction results is the uncertainty in the spectral calibration of the sensor. A typical problem is a constant spectral shift for all channels measured by a given spectrograph. This problem can be caused by a small mechanical misalignment of one or more optical elements in the system and can result in wavelength errors of several nm. The effects of wavelength shift errors are generally most severe in regions containing strong atmospheric absorption features. In these regions, spectral artifacts appear upon conversion of the radiance cube to a reflectance cube [117]. These demonstrate the importance and effect of in-flight calibration previously discussed in Section 2.3. In addition to spectral calibration, the radiometric calibration and SNR of imagery also pose a challenge to accurate atmospheric correction [24]. Some empirical models such as empirical line, which requires ground information give good results, so features and accuracy of ground measurements are crucial for final atmospheric correction result. Moreover, the changes in the environment during image acquisition have a great effect on atmospheric correction accuracy. The keys to radiative transfer models are the successful estimation of spatially variable information, especially columnar water vapor and aerosol optical thickness [118]. As the development of techniques and improvement of instrument performance evolve, surface reflectance accuracy after the atmospheric correction has been increasing, which promotes hyperspectral data application. Radiative transfer codes such as LOWTRAN, MODTRAN, 5S, and 6S were initially used to AVIRIS, but the results had a large deviation with ground measurements due to condition limitations [119]. A probabilistic formulation from optimal estimation inversion theory accounts for uncertainties in model parameters and measurement noise was applied to

AVIRIS-NG with analysis of retrieval accuracy and information content. The inversion outperformed traditional approaches, achieving a mean reflectance accuracy of 1% on diverse validation surfaces [51]. Additionally, a real-time visible shortwave infrared atmospheric correction performed onboard an aircraft by modifying the ATREM algorithm was first reported and applied to AVIRIS-NG [115]. MODTRAN-simulated Rayleigh and aerosol LUTs were designed specifically for the AISA for atmospheric correction, the retrieved surface reflectance agreed well with the input surface reflectance, with their relative difference <1% for most bands 400–700nm, but with blue bands exhibiting a large discrepancy between AISA-derived and field-measured reflectance possibly due to uncertainty in radiometric calibration [24]. The aerosol optical thickness and columnar water vapor were retrieved accurately for CASI-1500 and SASI-600 atmospheric correction based on a radiative transfer function, the derived surface reflectance correlated significantly with the ground spectra of comparable vegetation, cement road and soil targets [120]. HyMap data were atmospherically corrected using ATCOR 4, the accuracy of the deviation of ground measured reflectance and retrieved reflectance is up to 3 % [105].

3 Application

Airborne hyperspectral imaging spectrometers have been deployed for a wide range of scientific fields during the past thirty years [121–128]. In this paper, some new applications, novel model applications, and traditional applications variability are described with the improvement of instrument performance and hyperspectral data pre-processing technology in recent years.

3.1 CH₄ application

Some new objects detections have been carried out with the improvement of airborne hyperspectral imager performance, one prominent application is methane plume identification and quantification using AVIRIS-NG. Atmospheric methane is a long-lived greenhouse gas that absorbs LWIR radiation, which leads to global warming. Methane is also a precursor for tropospheric ozone and is strongly linked with co-emitted reactive trace gases that are the focus of air quality and public health policies, particularly in high priority regions. Since preindustrial times, the concentration of CH₄ in the atmosphere has increased by 150%, mainly due to fossil fuel and secondarily due to net land use change. Estimation of the global carbon budget is an important activity for a better understanding of the global carbon cycle and its effect on atmospheric warming [50]. High spatial and moderate spectral resolution AVIRIS-NG data was used for mapping the CH₄ source regions based on absorption spectroscopy features from 2.1–2.4 μm, as shown in Fig. 9 [129].

The American Jet Propulsion Laboratory (JPL) and partners have devised a tiered observational strategy for efficiently surveying large areas for methane point sources, quantifying individual source emissions, and estimating their contributions to the net emissions of key regions and sectors. Additionally, persistent monitoring of South Coast Air Basin total methane emissions by JPL's California laboratory for atmospheric remote sensing over 2011–2015 demonstrated the ability to assess variability in the emissions of a key region. It is worth noting is that methane retrievals were performed in real-time onboard the aircraft, which permits the instrument operator to identify and locate plumes in real-time, as shown in Fig. 10 [52]. During December 2015, a team from JPL, conducted an airborne campaign in active collaboration with the Indian Space Research Organization (ISRO), using the AVIRIS-NG payload, which was onboard ISRO's B200 Aircraft. These studies demonstrate the capability of AVIRIS-NG to quantify the column density of atmospheric species such as CH₄ over a region [50].

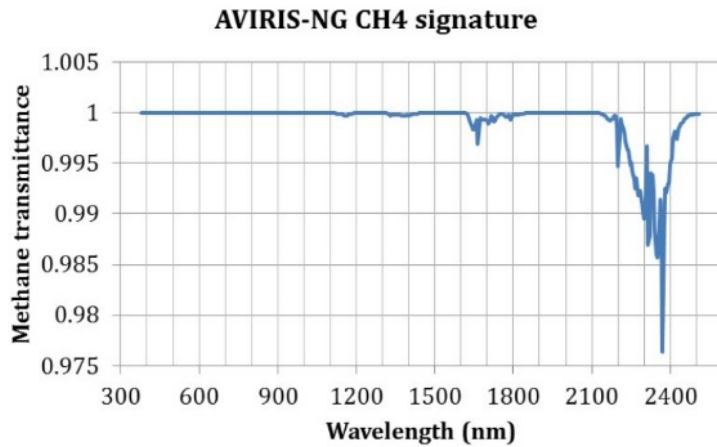


Fig. 9 Methane absorption signature (transmittance) plotted for the wavelength range measured by AVIRIS-NG. Strong absorptions are present between 2200 and 2450 nm.



Fig. 10 Real-time methane mapping onboard the aircraft. Red methane plumes are overlaid on raw AVIRIS-NG images with estimated peak enhancement (ppm-m) and plume source coordinates.

There are a number of key requirements for the airborne hyperspectral imaging system in order to detect and identify methane. First, the system must provide sufficient sensitivity to detect the phenomena of interest reliably. In other words, it must have sufficient SNR to find sources under the relevant wind, illumination, and substrate conditions. Only then can planners safely act on a null detection result. For similar reasons, it must minimize false positives. A second requirement is a high spatial resolution. The phenomena should subtend multiple pixels with sufficient resolution for the operator to identify typical morphologies. A third requirement is the data processing speed if a real-time operation is used. In addition, high accuracy spectral, radiometric, and geometric corrections are also necessary [52,130,131]. These key requirements are necessary for AVIRIS-NG to detect methane, since the performance of previous hyperspectral imager AVIRIS was not sufficient.

3.2 Broadband spectrum detection mode applications with high resolution

Earth objects and materials have different features observed in the VNIR, SWIR, and LWIR spectrum ranges. For example, within different spectral regions, specific or combined absorptions can be found, caused by the electronic transition of Fe-bearing minerals (VNIR region) and by the molecular vibration of specific chemical groups (e.g., OH⁻, CO₃, Si–O) (SWIR and LWIR spectral regions). Considering the main mineralogical groups, the VNIR parts of the electromagnetic (EMS) spectrum allow for mapping surfaces with a high concentration of Fe³⁺-bearing minerals (e.g., hematite, goethite and jarosite) [132–135] and SWIR is useful in detecting carbonates, clay minerals, and salts [136–138]. On the other hand, the VNIR and SWIR portions of the EMS are not optimal for detecting the main constituents of igneous rocks, quartz, and feldspars due to their lack of absorption features in the optical part of the EMS. These minerals can be mapped using the thermal LWIR region [139]. Different airborne hyperspectral sensors were combined for application or wide spectrum range spectrometers that were originally developed to detect new characterize materials. These wide spectrum applications modes composed of multiple instruments can defeat camouflage, more completely characterize occurrences, and improve qualification accuracy.

AHS, OMIS, and ARES are such instruments with a wide spectral range and can be applied to a specific scene, although their spatial and spectral resolution are not competitive. As shown in Fig. 11, roofs of different materials in Beijing city can be identified by composite images of multiple spectrum bands of OMIS. Three roofs in Fig. 11 (a) look the same in true color image of visible RGB due to the same blue paint on the outside, but the difference can be found by the false color composite images of the visible and infrared spectrum, as shown in Fig. 11 (b) and Fig. 11 (c). Fig. 12, which looks clearer because of higher ground sample distance (GSD), is another similar application acquired by FAHI in Changzhou city of China.

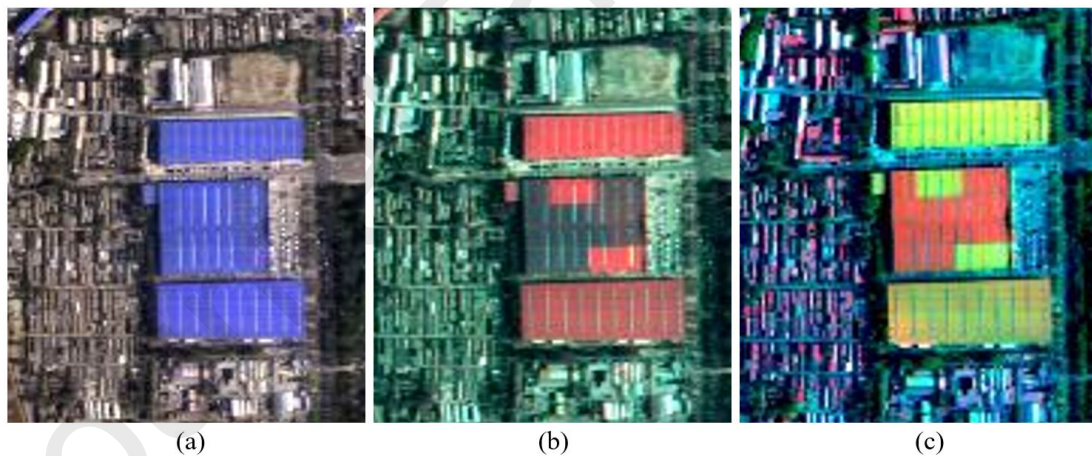


Fig. 11 The detection of roofs of different materials by OMIS in Beijing city. (a) True color image of visible (VIS) RGB. (b) False color composite images of VIS, near-infrared (NIR), and SWIR. (c) False color composite images of VIS, SWIR, and LWIR. The GSD is 3 m (3 mrad IFOV and 1000 m flight altitude).

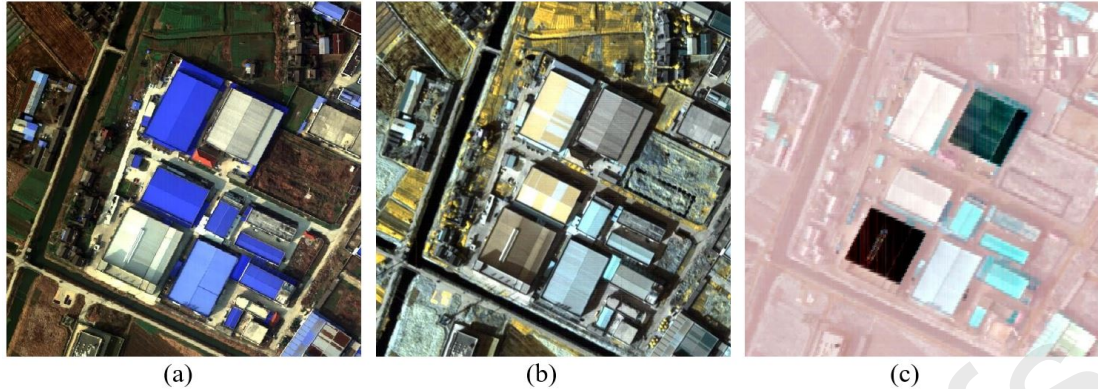


Fig. 12 The detection of roofs of different materials by FAHI in Changzhou city. (a) True color image of VIS RGB. (b) False color composite images of SWIR. (c) False color composite images of LWIR. The GSD is 0.375 m (0.25 mrad IFOV and 1500 m flight altitude).

The applications in Fig. 11 and Fig. 12 are visual qualitative identification and detection, although some mainstream airborne hyperspectral imagers have been integrated for quantitative analysis and application in recent years. For example, 1 m spatial resolution CASI (445.8–837.7 nm) imagery was used to classify Australian forest communities, and the integration of 2.6 m HyMap (446.1–2477.8 nm) spectra increased the accuracy of classification for some species, largely because of the inclusion of SWIR wavebands [140]. CASI and AHS images were used to estimate the fractional vegetation cover, which is an essential biophysical parameter for addressing land surface processes in the terrestrial climate system [141]. Two different airborne image datasets from HyMap (VNIR/SWIR image data) and AHS (LWIR image data) were analyzed, which took advantage of the data from wide spectral ranges. These different spectral ranges were interpreted separately. It was demonstrated that when the absorption feature information derived from multispectral LWIR data was integrated with the absorption feature information derived from hyperspectral VNIR/SWIR data, an important improvement in terms of more complex mineral mapping was achieved [139]. AVIRIS and spatially coincident HyTES data were used to map geology and alteration for a site in northern Death Valley, California and Nevada, USA. AVIRIS mapped iron oxides, clays, mica, and silicification (hydrothermal alteration), and the difference between calcite and dolomite. HyTES separated and mapped several igneous phases (not possible using AVIRIS), silicification, and validated separation of calcite from dolomite. Results illustrated that together, these two datasets provide an improved picture of the distribution of geologic units and subsequent alteration [53].

Although different airborne hyperspectral data have been combined for use, temporal decorrelation is also an issue, as most multimodal data are not collected simultaneously. This can be addressed by acquiring and analyzing temporally consistent datasets (acquired at the same time on the same platform with similar spatial resolution), such as CASI/SASI/TASI, SYSIPHE, and FAHI. CASI/SASI/TASI data was used to identify uranium mineralization factors, the spectral features of typical tetravalent, hexavalent uranium minerals and mineralization factors were established, and hyperspectral logging technology for drill cores and trenches also were developed, thus establishing the relationships between radioactive intensity and spectral characteristics [36]. The SYSIPHE system, which was built in collaboration between France and Norway, is to validate and quantify the interest of spectral imaging techniques for defense, security and environmental applications [21]. The FAHI, which is a Chinese next-generation pushbroom hyperspectral imager, has been successfully used for civilian and environmental monitoring [38]. Fig. 13 [57] shows the FAHI VNIR hyperspectral image of the island

with atoll. Fig. 13 (a) is a RGB image with R=670nm, G=560nm, B=470nm, and Fig. 13 (b) with R=600nm, G=480nm, B=430nm. Fig. 13 (c) is the reflectance curve of some typical targets. By choosing a proper RGB channel, desired targets can be easily enhanced in the image. Fig. 14 [57] shows the use of a plot of land in Xiong'an city of China using the image data obtained from the FAHI. With the spectral curve from the hyperspectral image, different elements are classified and identified, which shows the helpful of the hyperspectral imager in extracting crop growth information and protecting agricultural resources.

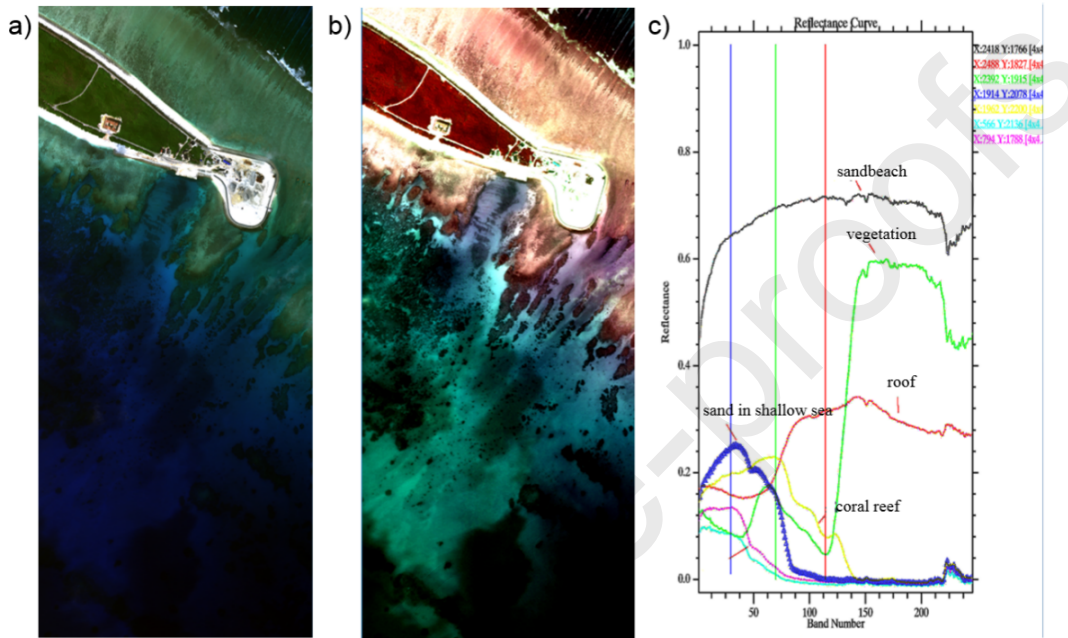


Fig. 13 FAHI VNIR hyperspectral image of island with atoll.

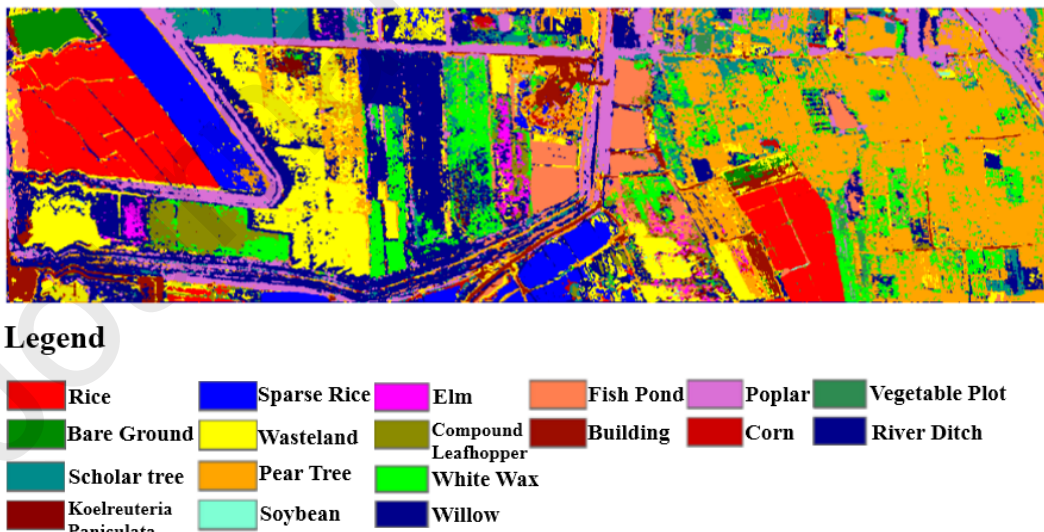


Fig. 14 Land classification map of FAHI.

3.3 Improvement of application accuracy

With the advance and maturity of technology, airborne hyperspectral imager performance and data preprocessing results have been improved, which largely promotes the improvement of application accuracy. APEX data was used to retrieve vegetation fluorescence (Fs) and in situ data were collected

using a stratified random sampling approach while measuring reflected and emitted radiances at each calibration point, resulting in a good agreement between APEX and in situ Fs ($R^2 = 0.87$) [28]. CASI and AHS were used to estimate the fractional vegetation cover, which is an essential biophysical parameter for addressing land surface processes in the terrestrial climate system, and a 97% of accuracy was obtained [141]. CASI data was used to map coral reef benthos, substrates, and bathymetry. Subsequent qualitative validation of these maps showed accurate mapping of areas dominated by sediment, benthic micro-algae, algal turf, live coral, and macro-algae. A bathymetric map was produced for water column depths 0.5–10 m, at 0.5 m intervals, and showed high correspondence with in-situ sonar data (R^2 value of 0.93) [142]. CASI/SASI/TASI hyperspectral data were used to studying the alteration characteristics to locate the possible hydrothermal/mineralization centers for the Baiyanghe uranium deposit, Xinjiang, NW China. The verification results show that the accuracy of mineral mapping of kaolinite and carbonate is nearly 100%, the accuracy of hematite is above 90%, and the accuracy of the three types of white mica and montmorillonite is above 85% [101]. Fine spatial resolution hyperspectral data collected from the HyMap was evaluated for both community and species-level vegetation mapping. Overall accuracy of 90% was obtained in discriminating 14 vegetation communities and an overall accuracy of 85% was achieved in identifying 55 species using an SVM model. HyMap imagery with synchronous in-situ spectral data was used to survey the environmental condition in Shenzhen of South China. The in-situ spectra were resampled in wavelength range and spectral resolution to that of HyMap sensor for image classification with the SAM algorithm. The unpaved granite interspersed with cement in paved mine pits, and newly excavated land surface and the eroded soil were mapped out with the accuracy over 95% [143].

3.4 Military application

The airborne hyperspectral imager is also important for many military applications in fields such as defeating camouflage, gathering information about battlespace, discrimination between targets and decoys, early warning for long-range missiles and space surveillance, detection of landmines and weapons of mass destruction, and monitoring of international treaty compliance [144–146]. Military applications and target detection projects may use hyperspectral sensors operating in both NIR and SWIR spectral bands to discriminate camouflage material from background vegetation. For example, hyperspectral imagery used by military personnel to detect military vehicles under partial vegetation canopy may make use of significant differences between camouflage and plant material in the SWIR spectral band based on differences in moisture content, which may not be apparent in other parts of the spectrum [147]. SYSIPHE requirements are based on both civilian and military applications. A flight campaign was led in September 2013, on the French air base of Cazaux. This site was chosen because the DGA-EV (French military flight test center) has a large active infrared target which allows - measuring in-flight radiometric and imaging performances of airborne infrared systems. The Cobra target is composed of independent panels to create controlled temperature patterns [20,21]. Fig. 15 shows an example of AVIRIS data with an airfield locating several aircraft. The targets were identified with a matched filter for the aircraft spectrum at the right of the figure [148].

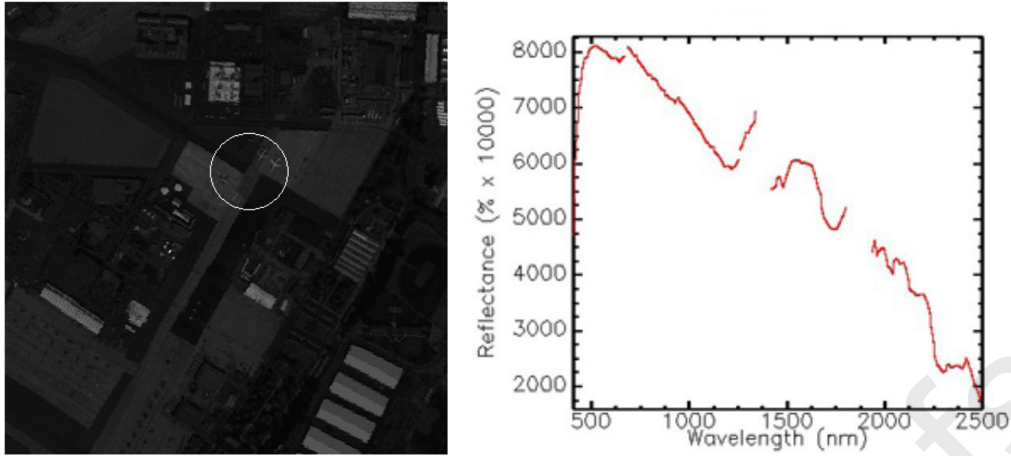


Fig. 15 Detection of aircraft with a matched filter approach.

4 Analysis and Discussion

With the maturity and development of technologies such as detector, optical system, mechanical structure, and electronics, airborne hyperspectral imagers are constantly being updated. AVIRIS was designed in 1987 and replaced by AVIRIS-NG in 2012. AISA was designed in 1992 and subsequent instruments were developed such as AISA+, AISA-DUAL (AISA-EAGLE and AISA-HAWK) [149], AISA-FENIX, and AISA-FENIX 1K, etc.. CASI was designed in 1989 and an advanced instrument designated as CASI-1500 was built [150], and then the composite of CASI, SASI, and TASI sensors was applied to many fields. APEX was designed in 1997 and the flight campaign was completed in 2008 [109]. The instrument has subsequently been improved and applied [28]. OMIS I and OMIS II were designed and implemented by the Shanghai Institute of Technical Physics (SITP), Chinese Academy of Sciences in the 90s, and a wider spectrum instrument FAHI was designed and implemented in 2016. These mainstream instruments were developed by different manufacturers and have different features and applications, e.g., AVIRIS-NG has higher performance than CASI-1500, but the latter, which was mainly designed for commercial application, has lower cost and weight.

In the past thirty years, airborne hyperspectral imaging technology has not only improved the instrument performance (spectral range, spatial and spectrum resolution, SNR, and FOV), but more importantly is the improvement of pre-processing accuracy such as calibration accuracy, geometric accuracy, and atmospheric correction accuracy, which have jointly promoted its development and application. The pushbroom imaging mode has become the main imaging mode of airborne hyperspectral imagers due to higher SNR compared with whiskbroom, but has the disadvantage of a small FOV, so multi-detector or multi-instrument stitching technology is used to increase the system FOV. Dispersive, FTI, and filter spectrometers are applied to airborne hyperspectral imagers. Grating spectrometers are used by most imagers because their spectral dispersion is linear. Silicon and MCT are the mainstream materials used in detectors for hyperspectral imagers. InAs/GaSb Type-II superlattices have proven to be an excellent material for high end infrared detectors in recent years. Thanks to the improvement of calibration technology, calibration accuracy has been increased, e.g., the spectral calibration accuracy of AVIRIS-NG is up to 0.1nm, the absolute radiometric accuracy is 5% and the linearity is better than 99%. IMU, GPS, and DTEM data are used in current geometric correction techniques, and numerous mature software packages have been applied. ATREM, ATCOR, FLAASH, HATCH, and ACORN software programs are available to model the atmosphere. Subsequently, atmospheric correction accuracy is also improved, e.g., AVIRIS-NG has achieved a mean reflectance accuracy of 1% on diverse validation surfaces. Thanks to the improvement of airborne hyperspectral imager performance and data pre-

processing accuracy, some new object detection and wide spectrum applications modes composed of multiple instruments have been carried out, and the application accuracy is largely improved.

Due to superior performance and flexibility, airborne hyperspectral imaging systems continue to play an important role in remote sensing applications. Satellite remote sensing provides synoptic and repeated measurements, but often suffers from cloud cover. Such difficulty may be overcome with airborne remote sensing when appropriate sensors and platforms are utilized. The airborne sensors are particularly useful for mapping coastal areas where spectral and spatial resolutions are more demanding than satellite sensors can provide. In addition, the spaceborne platform has disadvantages such as low spatial resolution (coarse mapping), performance degradation in the cloudy atmosphere, and onboard maintenance is not possible. For example, the ability of satellites to detect and quantify emissions from point sources is still limited to relatively coarse spatial scales. Some surface measurement networks and models can resolve methane fluxes at resolutions as fine as a few kilometers but so far this is limited to a few urban testbeds and in most cases is insufficient to pinpoint locations[129]. In addition to general applications, development and research, the airborne hyperspectral system has also been used to prototype and carry out experiments for satellite missions. Such as APEX, that was designed and applied to ESA Sentinels II and III, the evaluated Explorers Fluorescent Explorer and Tropospheric Composition and Air Quality, the German national initiative Advanced Hyperspectral Mission, and the South African Multi-Sensor Microsatellite Imager among others [22].

In summary, the airborne hyperspectral imager has rapidly evolved and is widely applied to many fields, but several challenges still exist that need to be resolved in the future. First, the instrument specifications, which contain wider spectral ranges and FOV, higher spatial, spectral resolution and SNR, need to result in advanced detectors. Meanwhile, the data quality, which mainly depends on the results of calibration, geometric and atmosphere correction accuracies, must be guaranteed. Furthermore, specialized spectrometers can be designed specifically for the purposes of the application. For example, an imaging spectrometer, which focused just on the 2.1–2.4 μm range, would offer far better detection performance and permit much finer spectral resolution for highly sensitive and accurate retrievals for CH₄ detection. In addition, upcoming unmanned aerial vehicle (UAV) platforms can provide slower and lower flying platforms, which would provide higher spatial resolution and improved SNR. New inexpensive sensors can be designed for UAV platforms. Third, hyperspectral imaging is also becoming a big data issue due to the large amounts of data and bands collected by sensors. High speed and real-time processing technology will be increasingly needed, especially for military applications.

5 Conclusion

With the development of hyperspectral imaging technology, the airborne hyperspectral imager performance is improved greatly. It is widely used for both civilian and military applications. Some key technologies such as high data throughput imaging modes, high quality spectroscopic subsystem, and high sensitivity detector technology were discussed in this paper. In addition, pre-processing procedures composed of calibration, geometric rectification and atmosphere correction based on currently mainstream airborne hyperspectral imagers were described in detail. These technologies and procedures are important for meeting the requirement of acquiring high accuracy surface reflectance data and are the key factors for the characterization and quantification of hyperspectral imaging.

The key technologies of some mainstream airborne hyperspectral imagers such as AISA-FENIX, AISA, APEX, AVIRIS-NG, CASI/SASI/TASI, FAHI, and SYSIPHE were described in detail. FAHI developed by SITP, is a Chinese next generation pushbroom hyperspectral imager with features of high spatial resolution, high spectral resolution, wide spectrum range, and large FOV. It has been successfully

used for civilian and environmental monitoring and completed 7 s flight experiments in China. The cost per flight, which includes flight fees, instrument depreciation, and labor costs, is about 300 thousand yuan (44,567 dollars) and 4–5 terabytes data can be obtained in 1–3 kilometers flight altitudes.

CH₄ detection and broadband spectrum detection mode applications with high resolution in recent years were introduced. The detection and identification of methane demonstrates the performance of AVIRIS-NG with high spatial resolution and SNR. Although the improvement of airborne hyperspectral imaging systems has greatly enhanced application accuracy, challenges still exist in instrument performance, new application exploration, and data processing speed.

This compilation of hyperspectral imagers used in airborne missions can be serve as an important reference to designers of future airborne hyperspectral systems and researchers who evaluate the data precision of different airborne hyperspectral sensors.

REFERENCES

- [1] V.V. Kozoderov, T.V. Kondranin, E.V. Dmitriev, V.P. Kamentsev, A system for processing hyperspectral imagery: application to detecting forest species, *International Journal of Remote Sensing.* 35 (2014) 5926–5945. doi:10.1080/01431161.2014.944997.
- [2] S. Lohumi, S. Lee, H. Lee, M.S. Kim, W.-H. Lee, B.-K. Cho, Application of hyperspectral imaging for characterization of intramuscular fat distribution in beef, *Infrared Physics & Technology.* 74 (2016) 1–10. doi:10.1016/j.infrared.2015.11.004.
- [3] D. Kimuli, W. Wang, W. Wang, H. Jiang, X. Zhao, X. Chu, Application of SWIR hyperspectral imaging and chemometrics for identification of aflatoxin B1 contaminated maize kernels, *Infrared Physics & Technology.* 89 (2018) 351–362. doi:10.1016/j.infrared.2018.01.026.
- [4] A. Ambrose, L.M. Kandpal, M.S. Kim, W.H. Lee, B.K. Cho, High speed measurement of corn seed viability using hyperspectral imaging, *Infrared Physics & Technology.* 75 (2016) 173–179. doi:10.1016/j.infrared.2015.12.008.
- [5] H. He, D. Sun, Hyperspectral imaging technology for rapid detection of various microbial contaminants in agricultural and food products, *Trends in Food Science & Technology.* 46 (2015) 99–109. doi:10.1016/j.tifs.2015.08.001.
- [6] K. Randolph, J. Wilson, L. Tedesco, L. Li, D.L. Pascual, E. Soyeux, Hyperspectral remote sensing of cyanobacteria in turbid productive water using optically active pigments, chlorophyll a and phycocyanin, *Remote Sensing of Environment.* 112 (2008) 4009–4019. doi:10.1016/j.rse.2008.06.002.
- [7] D. Zhang, Y. Xu, W. Huang, X. Tian, Y. Xia, L. Xu, S. Fan, Nondestructive measurement of soluble solids content in apple using near infrared hyperspectral imaging coupled with wavelength selection algorithm, *Infrared Physics & Technology.* 98 (2019) 297–304. doi:10.1016/j.infrared.2019.03.026.
- [8] D. Liu, X. Zeng, D. Sun, Recent Developments and Applications of Hyperspectral Imaging for Quality Evaluation of Agricultural Products: A Review, *Critical Reviews in Food Science and Nutrition.* 55 (2015) 1744–1757. doi:10.1080/10408398.2013.777020.
- [9] H. Huang, L. Liu, M.O. Ngadi, Recent developments in hyperspectral imaging for assessment of food quality and safety, *Sensors.* 14 (2014) 7248–7276. doi:10.3390/s140407248.
- [10] C. Jing, Y. Bokun, W. Runsheng, T. Feng, Z. Yingjun, L. Dechang, Y. Suming, S. Wei, Regional-scale mineral mapping using ASTER VNIR/SWIR data and validation of reflectance and mineral map products using airborne hyperspectral CASI/SASI data, *International Journal of Applied Earth Observation and Geoinformation.* 33 (2014) 127–141. doi:10.1016/j.jag.2014.04.014.

- [11] L. Wei, X. Xiao, Y. Wang, X. Zhuang, J. Wang, Research on the shortwave infrared hyperspectral imaging technology based on Integrated Stepwise filter, *Infrared Physics & Technology.* 86 (2017) 90–97. doi:10.1016/j.infrared.2017.08.023.
- [12] V.E. Brando, A.G. Dekker, Satellite hyperspectral remote sensing for estimating estuarine and coastal water quality, *IEEE Transactions on Geoscience and Remote Sensing.* 41 (2003) 1378–1387. doi:10.1109/TGRS.2003.812907.
- [13] C. Erkinbaev, K. Derksen, J. Paliwal, Single kernel wheat hardness estimation using near infrared hyperspectral imaging, *Infrared Physics & Technology.* 98 (2019) 250–255. doi:10.1016/j.infrared.2019.03.033.
- [14] M. Jhabvala, S. Gunapala, D. Reuter, K.K. Choi, S. Bandara, J. Liu, A. La, S. Banks, J. Cho, T. Hwang, S. Tsay, D. Rafol, H. Huet, N. Chauvet, T. Huss, Development of a 4–15 μm infrared GaAs hyperspectral QWIP imager, *Infrared Physics & Technology.* 44 (2003) 445–455. doi:10.1016/S1350-4495(03)00172-5.
- [15] S. Yang, Z. Song, H. Yuan, Z. Zou, Z. Shi, Fast high-order matched filter for hyperspectral image target detection, *Infrared Physics & Technology.* 94 (2018) 151–155. doi:10.1016/j.infrared.2018.09.018.
- [16] M. Shimoni, R. Haelterman, C. Perneel, Hypersectral Imaging for Military and Security Applications: Combining Myriad Processing and Sensing Techniques, *IEEE Geoscience and Remote Sensing Magazine.* 7 (2019) 101–117. doi:10.1109/MGRS.2019.2902525.
- [17] Heesung Kwon, N.M. Nasrabadi, Kernel RX-algorithm: a nonlinear anomaly detector for hyperspectral imagery, *IEEE Transactions on Geoscience and Remote Sensing.* 43 (2005) 388–397. doi:10.1109/TGRS.2004.841487.
- [18] C. Ke, Military object detection using multiple information extracted from hyperspectral imagery, in: 2017 International Conference on Progress in Informatics and Computing (PIC), 2017: pp. 124–128. doi:10.1109/PIC.2017.8359527.
- [19] M.D. Farrell, R.M. Mersereau, On the impact of PCA dimension reduction for hyperspectral detection of difficult targets, *IEEE Geoscience and Remote Sensing Letters.* 2 (2005) 192–195. doi:10.1109/LGRS.2005.846011.
- [20] C. Coudrain, S. Bernhardt, M. Caes, R. Domel, Y. Ferrec, R. Gouyon, D. Henry, M. Jacquot, A. Kattnig, P. Perrault, L. Poutier, L. Rousset-Rouvière, M. Tauvy, S. Thétas, J. Primot, SIELETERS, an airborne infrared dual-band spectro-imaging system for measurement of scene spectral signatures, *Opt. Express, OE.* 23 (2015) 16164–16176. doi:10.1364/OE.23.016164.
- [21] L.R. Rouvière, I. Sisakoun, T. Skauli, C. Coudrain, Y. Ferrec, S. Fabre, L. Poutier, Y. Boucher, T. Løke, S. Blaaberg, Sysiphe, an airborne hyperspectral system from visible to thermal infrared, in: 2016 IEEE International Geoscience and Remote Sensing Symposium (IGARSS), 2016: pp. 1947–1949. doi:10.1109/IGARSS.2016.7729501.
- [22] K.I. Itten, F. Dell’Endice, A. Hueni, M. Kneubühler, D. Schläpfer, D. Odermatt, F. Seidel, S. Huber, J. Schopfer, T. Kellenberger, Y. Bühl, P. D’Odorico, J. Nieke, E. Alberti, K. Meuleman, APEX - the Hyperspectral ESA Airborne Prism Experiment, *Sensors.* 8 (2008) 6235–6259. doi:10.3390/s8106235.
- [23] C. Hu, K.L. Carder, Atmospheric correction for airborne sensors: Comment on a scheme used for CASI, *Remote Sensing of Environment.* 79 (2002) 134–137. doi:10.1016/S0034-4257(01)00232-2.
- [24] M. Zhang, C. Hu, D. English, P. Carlson, F.E. Muller-Karger, G. Toro-Farmer, S.R. Herwitz,

- Atmospheric Correction of AISA Measurements Over the Florida Keys Optically Shallow Waters: Challenges in Radiometric Calibration and Aerosol Selection, *IEEE Journal of Selected Topics in Applied Earth Observations and Remote Sensing.* 8 (2015) 4189–4196. doi:10.1109/JSTARS.2015.2437326.
- [25] G. Vane, A.F.H. Goetz, J.B. Wellman, Airborne imaging spectrometer: A new tool for remote sensing, *IEEE Transactions on Geoscience and Remote Sensing.* GE-22 (1984) 546–549. doi:10.1109/TGRS.1984.6499168.
 - [26] J.A. Sobrino, J.C. JiménezMuñoz, P.J. ZarcoTejada, G. SepulcreCantó, E. de Miguel, Land surface temperature derived from airborne hyperspectral scanner thermal infrared data, *Remote Sensing of Environment.* 102 (2006) 99–115. doi:10.1016/j.rse.2006.02.001.
 - [27] D. Rogge, B. Rivard, K. Segl, B. Grant, J. Feng, Mapping of NiCu–PGE ore hosting ultramafic rocks using airborne and simulated EnMAP hyperspectral imagery, Nunavik, Canada, *Remote Sensing of Environment.* 152 (2014) 302–317. doi:10.1016/j.rse.2014.06.024.
 - [28] M.E. Schaepman, M. Jehle, A. Hueni, P. D'Odorico, A. Damm, J. Weyermann, F.D. Schneider, V. Laurent, C. Popp, F.C. Seidel, K. Lenhard, P. Gege, C. Küchler, J. Brazile, P. Kohler, L. De Vos, K. Meuleman, R. Meynart, D. Schläpfer, M. Kneubühler, K.I. Itten, Advanced radiometry measurements and Earth science applications with the Airborne Prism Experiment (APEX), *Remote Sensing of Environment.* 158 (2015) 207–219. doi:10.1016/j.rse.2014.11.014.
 - [29] A. Muller, R. Richter, M. Habermeyer, S. Dech, K. Segl, H. Kaufmann, Spectroradiometric requirements for the reflective module of the airborne spectrometer ARES, *IEEE Geoscience and Remote Sensing Letters.* 2 (2005) 329–332. doi:10.1109/LGRS.2005.848513.
 - [30] L.R. Gaddis, L.A. Soderblom, H.H. Kieffer, K.J. Becker, J. Torson, K. Mullins, Decomposition of AVIRIS spectra: extraction of surface-reflectance, atmospheric, and instrumental components, *IEEE Transactions on Geoscience and Remote Sensing.* 34 (1996) 163–178. doi:10.1109/36.481901.
 - [31] A. Plaza, P. Martinez, J. Plaza, R. Perez, Dimensionality reduction and classification of hyperspectral image data using sequences of extended morphological transformations, *IEEE Transactions on Geoscience and Remote Sensing.* 43 (2005) 466–479. doi:10.1109/TGRS.2004.841417.
 - [32] B. Hörig, F. Kühn, F. Oschütz, F. Lehmann, HyMap hyperspectral remote sensing to detect hydrocarbons, *International Journal of Remote Sensing.* 22 (2001) 1413–1422. doi:10.1080/01431160120909.
 - [33] R.G. Resmini, M.E. Kappus, W.S. Aldrich, J.C. Harsanyi, M. Anderson, Mineral mapping with HYperspectral Digital Imagery Collection Experiment (HYDICE) sensor data at Cuprite, Nevada, U.S.A., *International Journal of Remote Sensing.* 18 (1997) 1553–1570. doi:10.1080/014311697218278.
 - [34] E. Belluco, M. Camuffo, S. Ferrari, L. Modenese, S. Silvestri, A. Marani, M. Marani, Mapping salt-marsh vegetation by multispectral and hyperspectral remote sensing, *Remote Sensing of Environment.* 105 (2006) 54–67. doi:10.1016/j.rse.2006.06.006.
 - [35] P. Du, K. Tan, H. Su, Feature extraction for target identification and image classification of OMIS hyperspectral image, *Mining Science and Technology (China).* 19 (2009) 835–841. doi:10.1016/S1674-5264(09)60152-6.
 - [36] Z. Jielin, W. Junhu, Z. Mi, H. Yanju, W. Ding, Aerial visible-thermal infrared hyperspectral feature extraction technology and its application to object identification, *IOP Conf. Ser.: Earth Environ.*

- Sci. 17 (2014) 012184. doi:10.1088/1755-1315/17/1/012184.
- [37] S.J. Edberg, D.L. Evans, J.E. Graf, J.J. Hyon, P.A. Rosen, D.E. Waliser, Studying Earth in the New Millennium: NASA Jet Propulsion Laboratory's Contributions to Earth Science and Applications Space Agencies, *IEEE Geoscience and Remote Sensing Magazine*. 4 (2016) 26–39. doi:10.1109/MGRS.2016.2525678.
- [38] J. Jia, Y. Wang, X. Cheng, L. Yuan, D. Zhao, Q. Ye, X. Zhuang, R. Shu, J. Wang, Destriping Algorithms Based on Statistics and Spatial Filtering for Visible-to-Thermal Infrared Pushbroom Hyperspectral Imagery, *IEEE Transactions on Geoscience and Remote Sensing*. 57 (2019) 4077–4091. doi:10.1109/TGRS.2018.2889731.
- [39] S. Meerdink, D. Roberts, G. Hulley, P. Gader, J. Pisek, K. Adamson, J. King, S.J. Hook, Plant species' spectral emissivity and temperature using the hyperspectral thermal emission spectrometer (HyTES) sensor, *Remote Sensing of Environment*. 224 (2019) 421–435. doi:10.1016/j.rse.2019.02.009.
- [40] S.J. Hook, W.R. Johnson, M.J. Abrams, NASA's Hyperspectral Thermal Emission Spectrometer (HyTES), in: C. Kuenzer, S. Dech (Eds.), *Thermal Infrared Remote Sensing: Sensors, Methods, Applications*, Springer Netherlands, Dordrecht, 2013: pp. 93–115. doi:10.1007/978-94-007-6639-6_5.
- [41] N. Carmon, E. Ben-Dor, Mapping Asphaltic Roads' Skid Resistance Using Imaging Spectroscopy, *Remote Sensing*. 10 (2018) 430. doi:10.3390/rs10030430.
- [42] R.O. Green, C. Team, New measurements of the earth's spectroscopic diversity acquired during the aviris-*ng* campaign to India, in: 2017 IEEE International Geoscience and Remote Sensing Symposium (IGARSS), 2017: pp. 3066–3069. doi:10.1109/IGARSS.2017.8127646.
- [43] CASI-1500, ITRES. (n.d.). <http://www.itres.com/casi-1500/> (accessed September 5, 2019).
- [44] SASI-1000A, ITRES. (n.d.). <http://www.itres.com/sasi-1000a/> (accessed September 5, 2019).
- [45] TASI-600, ITRES. (n.d.). <http://www.itres.com/tasi-600/> (accessed September 5, 2019).
- [46] X. Cheng, Y. Wang, R. Guo, J. Huang, Unsupervised classification-based hyperspectral data processing: lossy compression, *Opt Quant Electron*. 50 (2018) 457. doi:10.1007/s11082-018-1686-7.
- [47] S. Chang, H. Syu, Y. Wang, C. Lai, S. Huang, H. Wang, Identifying the incidence level of periodontal disease through hyperspectral imaging, *Opt Quant Electron*. 50 (2018) 409. doi:10.1007/s11082-018-1678-7.
- [48] Y. Liu, L. Yang, F. Chen, Multispectral registration method based on stellar trajectory fitting, *Opt Quant Electron*. 50 (2018) 189. doi:10.1007/s11082-018-1458-4.
- [49] D.S. Matheson, P.E. Dennison, Evaluating the effects of spatial resolution on hyperspectral fire detection and temperature retrieval, *Remote Sensing of Environment*. 124 (2012) 780–792. doi:10.1016/j.rse.2012.06.026.
- [50] M. Pathakoti, B. Gharai, S. Gaddamidi, R.P.V. Narshimha, M. Kapanaboina, S.V.R. Mullapudi, K.M.V.N. Yelisetty, Estimation of molecular column density of methane (XCH4) using AVIRIS-NG data, *JARS*. 12 (2018) 046005. doi:10.1111/1.JRS.12.046005.
- [51] D.R. Thompson, V. Natraj, R.O. Green, M.C. Helmlinger, B.-C. Gao, M.L. Eastwood, Optimal estimation for imaging spectrometer atmospheric correction, *Remote Sensing of Environment*. 216 (2018) 355–373. doi:10.1016/j.rse.2018.07.003.
- [52] D.R. Thompson, I. Leifer, H. Bovensmann, M. Eastwood, M. Fladeland, C. Frankenberg, K. Gerilowski, R.O. Green, S. Kratwurst, T. Krings, B. Luna, A.K. Thorpe, Real-time remote

- detection and measurement for airborne imaging spectroscopy: a case study with methane, *Atmospheric Measurement Techniques*. 8 (2015) 4383–4397. doi:<https://doi.org/10.5194/amt-8-4383-2015>.
- [53] F.A. Kruse, Comparative analysis of Airborne Visible/Infrared Imaging Spectrometer (AVIRIS), and Hyperspectral Thermal Emission Spectrometer (HyTES) longwave infrared (LWIR) hyperspectral data for geologic mapping, in: *Algorithms and Technologies for Multispectral, Hyperspectral, and Ultraspectral Imagery XXI*, International Society for Optics and Photonics, 2015: p. 94721F. doi:[10.1117/12.2176646](https://doi.org/10.1117/12.2176646).
 - [54] J. Jia, Y. Wang, X. Zhuang, Y. Yao, S. Wang, D. Zhao, R. Shu, J. Wang, High spatial resolution shortwave infrared imaging technology based on time delay and digital accumulation method, *Infrared Physics & Technology*. 81 (2017) 305–312. doi:[10.1016/j.infrared.2017.01.017](https://doi.org/10.1016/j.infrared.2017.01.017).
 - [55] J. Lang, Y. Wang, X. Xiao, X. Zhuang, S. Wang, J. Liu, J. Wang, Study on shortwave infrared long-distance imaging performance based on multiband imaging experiments, *OE*. 52 (2013) 045008. doi:[10.1117/1.OE.52.4.045008](https://doi.org/10.1117/1.OE.52.4.045008).
 - [56] P.J. Curran, J.L. Dungan, Estimation of signal-to-noise: a new procedure applied to AVIRIS data, *IEEE Transactions on Geoscience and Remote Sensing*. 27 (1989) 620–628. doi:[10.1109/TGRS.1989.35945](https://doi.org/10.1109/TGRS.1989.35945).
 - [57] D. Zhang, L. Yuan, S. Wang, H. Yu, C. Zhang, D. He, G. Han, J. Wang, Y. Wang, Wide Swath and High Resolution Airborne HyperSpectral Imaging System and Flight Validation, *Sensors*. 19 (2019) 1667. doi:[10.3390/s19071667](https://doi.org/10.3390/s19071667).
 - [58] Z. He, B. Wang, G. Lü, C. Li, L. Yuan, R. Xu, B. Liu, K. Chen, J. Wang, Operating principles and detection characteristics of the Visible and Near-Infrared Imaging Spectrometer in the Chang'e-3, *Research in Astronomy and Astrophysics*. 14 (2014) 1567–1577. doi:<https://doi.org/10.1088/1674-4527/14/12/006>.
 - [59] Z.P. He, B.Y. Wang, G. Lv, C.L. Li, L.Y. Yuan, R. Xu, K. Chen, J.Y. Wang, Visible and near-infrared imaging spectrometer and its preliminary results from the Chang'E 3 project, *Review of Scientific Instruments*. 85 (2014) 083104. doi:[10.1063/1.4891865](https://doi.org/10.1063/1.4891865).
 - [60] J. Brazile, R.A. Neville, K. Staenz, D. Schlapfer, Lixin Sun, K.I. Itten, Scene-based spectral response function shape discernibility for the APEX imaging spectrometer, *IEEE Geoscience and Remote Sensing Letters*. 3 (2006) 414–418. doi:[10.1109/LGRS.2006.873873](https://doi.org/10.1109/LGRS.2006.873873).
 - [61] M. Wen, Y. Wang, Y. Yao, L. Yuan, S. Zhou, J. Wang, Design and performance of curved prism-based mid-wave infrared hyperspectral imager, *Infrared Physics & Technology*. 95 (2018) 5–11. doi:[10.1016/j.infrared.2018.10.001](https://doi.org/10.1016/j.infrared.2018.10.001).
 - [62] Hyperspectral Remote Sensing - Specim Spectral Imaging Ltd., Specim, Spectral Imaging Ltd. (n.d.). <https://www.specim.fi/hyperspectral-remote-sensing/> (accessed September 7, 2019).
 - [63] A. Fridman, G. Høye, T. Løke, Resampling in hyperspectral cameras as an alternative to correcting keystone in hardware, with focus on benefits for optical design and data quality, *OE*. 53 (2014) 053107. doi:[10.1117/1.OE.53.5.053107](https://doi.org/10.1117/1.OE.53.5.053107).
 - [64] B. Fièque, P. Chorier, B. Terrier, Sofradir detectors for hyperspectral applications from visible up to VLWIR, in: *Sensors, Systems, and Next-Generation Satellites XIV*, International Society for Optics and Photonics, 2010: p. 78261I. doi:[10.1117/12.865044](https://doi.org/10.1117/12.865044).
 - [65] W. Hu, Z. Ye, L. Liao, H. Chen, L. Chen, R. Ding, L. He, X. Chen, W. Lu, 128 long-wavelength/mid-wavelength two-color HgCdTe infrared focal plane array detector with ultralow spectral cross talk, *Opt. Lett.*, OL. 39 (2014) 5184–5187. doi:[10.1364/OL.39.005184](https://doi.org/10.1364/OL.39.005184).

- [66] P. Wang, Y. Wang, M. Wu, Z. Ye, A junction-level optoelectronic characterization of etching-induced damage for third-generation HgCdTe infrared focal-plane array photodetectors, *Infrared Physics & Technology.* 91 (2018) 119–122. doi:10.1016/j.infrared.2017.12.007.
- [67] Y. Li, W. Hu, Z. Ye, Y. Chen, X. Chen, W. Lu, Direct mapping and characterization of dry etch damage-induced PN junction for long-wavelength HgCdTe infrared detector arrays, *Opt. Lett., OL.* 42 (2017) 1325–1328. doi:10.1364/OL.42.001325.
- [68] Q. Li, J. He, W. Hu, L. Chen, X. Chen, W. Lu, Influencing Sources for Dark Current Transport and Avalanche Mechanisms in Planar and Mesa HgCdTe p-i-n Electron-Avalanche Photodiodes, *IEEE Transactions on Electron Devices.* 65 (2018) 572–576. doi:10.1109/TED.2017.2783352.
- [69] M. Long, P. Wang, H. Fang, W. Hu, Progress, Challenges, and Opportunities for 2D Material Based Photodetectors, *Advanced Functional Materials.* 29 (2019) 1803807. doi:10.1002/adfm.201803807.
- [70] J. Wang, H. Fang, X. Wang, X. Chen, W. Lu, W. Hu, Recent Progress on Localized Field Enhanced Two-dimensional Material Photodetectors from Ultraviolet—Visible to Infrared, *Small.* 13 (2017) 1700894. doi:10.1002/smll.201700894.
- [71] Y. Ferrec, S. Théas, J. Primot, C. Coudrain, P. Perrault, P. Fournet, S. Bernhardt, M. Caës, M. Tauvy, J. Deschamps, D. Henry, A. Kattnig, P. Cymbalista, L. Rousset-Rouvière, Sieleters, an airborne Imaging Static Fourier Transform Spectrometer: design and preliminary laboratory results, in: *Imaging and Applied Optics* (2013), Paper FM1D.3, Optical Society of America, 2013: p. FM1D.3. doi:10.1364/FTS.2013.FM1D.3.
- [72] R. Green, 30 Years of Thermally Controlled Imaging Spectrometers for Earth and Planetary Science, (2016). <https://ttu-ir.tdl.org/handle/2346/67506> (accessed September 6, 2019).
- [73] P. D’Odorico, E. Alberti, M.E. Schaepman, In-flight spectral performance monitoring of the Airborne Prism Experiment, *Appl. Opt., AO.* 49 (2010) 3082–3091. doi:10.1364/AO.49.003082.
- [74] A. Rogalski, P. Martyniuk, InAs/GaInSb superlattices as a promising material system for third generation infrared detectors, *Infrared Physics & Technology.* 48 (2006) 39–52. doi:10.1016/j.infrared.2005.01.003.
- [75] L. Höglund, C. Asplund, R. Marcks von Würtemberg, H. Kataria, A. Gamfeldt, S. Smuk, H. Martijn, E. Costard, Manufacturability of type-II InAs/GaSb superlattice detectors for infrared imaging, *Infrared Physics & Technology.* 84 (2017) 28–32. doi:10.1016/j.infrared.2017.03.002.
- [76] X. Zhou, D. Li, J. Huang, Y. Zhang, Y. Mu, W. Ma, X. Tie, D. Zuo, Mid-wavelength type II InAs/GaSb superlattice infrared focal plane arrays, *Infrared Physics & Technology.* 78 (2016) 263–267. doi:10.1016/j.infrared.2016.08.014.
- [77] D.R. Rhiger, R.E. Kvaas, S.F. Harris, C.J. Hill, Characterization of LWIR diodes on InAs/GaSb Type-II superlattice material, *Infrared Physics & Technology.* 52 (2009) 304–309. doi:10.1016/j.infrared.2009.05.009.
- [78] P.M. Teillet, G. Fedosejevs, R.P. Gauthier, N.T. O'Neill, K.J. Thome, S.F. Biggar, H. Ripley, A. Meygret, A generalized approach to the vicarious calibration of multiple Earth observation sensors using hyperspectral data, *Remote Sensing of Environment.* 77 (2001) 304–327. doi:10.1016/S0034-4257(01)00211-5.
- [79] J. Secker, K. Staenz, R.P. Gauthier, P. Budkewitsch, Vicarious calibration of airborne hyperspectral sensors in operational environments, *Remote Sensing of Environment.* 76 (2001) 81–92. doi:10.1016/S0034-4257(00)00194-2.
- [80] N. Zhang, X. Zhang, G. Yang, C. Zhu, L. Huo, H. Feng, Assessment of defoliation during the

- Dendrolimus tabulaeformis Tsai et Liu disaster outbreak using UAV-based hyperspectral images, *Remote Sensing of Environment*. 217 (2018) 323–339. doi:10.1016/j.rse.2018.08.024.
- [81] A. Hueni, K. Lenhard, A. Baumgartner, M.E. Schaepman, Airborne Prism Experiment Calibration Information System, *IEEE Transactions on Geoscience and Remote Sensing*. 51 (2013) 5169–5180. doi:10.1109/TGRS.2013.2246575.
 - [82] R.O. Green, B.E. Pavri, T.G. Chrien, On-orbit radiometric and spectral calibration characteristics of EO-1 Hyperion derived with an underflight of AVIRIS and in situ measurements at Salar de Arizaro, Argentina, *IEEE Transactions on Geoscience and Remote Sensing*. 41 (2003) 1194–1203. doi:10.1109/TGRS.2003.813204.
 - [83] R.O. Green, Spectral calibration requirement for Earth-looking imaging spectrometers in the solar-reflected spectrum, *Appl. Opt.*, AO. 37 (1998) 683–690. doi:10.1364/AO.37.000683.
 - [84] R.O. Green, T.G. Chrien, P.J. Nielson, C.M. Sarture, B.T. Eng, C. Chovit, A.T. Murray, M.L. Eastwood, H.I. Novack, Airborne visible/infrared imaging spectrometer (AVIRIS): recent improvements to the sensor and data facility, in: *Imaging Spectrometry of the Terrestrial Environment*, International Society for Optics and Photonics, 1993: pp. 180–190. doi:10.1117/12.157056.
 - [85] M. Jehle, A. Hueni, K. Lenhard, A. Baumgartner, M.E. Schaepman, Detection and Correction of Radiance Variations During Spectral Calibration in APEX, *IEEE Geoscience and Remote Sensing Letters*. 12 (2015) 1023–1027. doi:10.1109/LGRS.2014.2374358.
 - [86] Y. Duan, W. Chen, M. Wang, L. Yan, A Relative Radiometric Correction Method for Airborne Image Using Outdoor Calibration and Image Statistics, *IEEE Transactions on Geoscience and Remote Sensing*. 52 (2014) 5164–5174. doi:10.1109/TGRS.2013.2287029.
 - [87] X. Lu, Y. Wang, Y. Yuan, Graph-Regularized Low-Rank Representation for Destriping of Hyperspectral Images, *IEEE Transactions on Geoscience and Remote Sensing*. 51 (2013) 4009–4018. doi:10.1109/TGRS.2012.2226730.
 - [88] X. Cheng, X. Zhuang, D. Zhang, Y. Yao, J. Hou, D. He, J. Jia, Y. Wang, A relative radiometric correction method for airborne SWIR hyperspectral image using the side-slither technique, *Opt Quant Electron*. 51 (2019) 105. doi:10.1007/s11082-019-1816-x.
 - [89] Jinsong Chen, Yun Shao, Huadong Guo, Weiming Wang, Boqin Zhu, Destriping CMODIS data by power filtering, *IEEE Transactions on Geoscience and Remote Sensing*. 41 (2003) 2119–2124. doi:10.1109/TGRS.2003.817206.
 - [90] J.G. Liu, G.L.K. Morgan, FFT Selective and Adaptive Filtering for Removal of Systematic Noise in ETM+ Imageodesy Images, *IEEE Transactions on Geoscience and Remote Sensing*. 44 (2006) 3716–3724. doi:10.1109/TGRS.2006.881752.
 - [91] P. Rakwatin, W. Takeuchi, Y. Yasuoka, Stripe Noise Reduction in MODIS Data by Combining Histogram Matching With Facet Filter, *IEEE Transactions on Geoscience and Remote Sensing*. 45 (2007) 1844–1856. doi:10.1109/TGRS.2007.895841.
 - [92] M. WEGENER, Destriping multiple sensor imagery by improved histogram matching, *International Journal of Remote Sensing*. 11 (1990) 859–875. doi:10.1080/01431169008955060.
 - [93] F.L. Gadallah, F. Csillag, E.J.M. Smith, Destriping multisensor imagery with moment matching, *International Journal of Remote Sensing*. 21 (2000) 2505–2511. doi:10.1080/01431160050030592.
 - [94] G. Corsini, M. Diani, T. Walzel, Striping removal in MOS-B data, *IEEE Transactions on Geoscience and Remote Sensing*. 38 (2000) 1439–1446. doi:10.1109/36.843038.
 - [95] G. Liu, Z. Lin, S. Yan, J. Sun, Y. Yu, Y. Ma, Robust Recovery of Subspace Structures by Low-

- Rank Representation, *IEEE Transactions on Pattern Analysis and Machine Intelligence*. 35 (2013) 171–184. doi:10.1109/TPAMI.2012.88.
- [96] C. Lang, G. Liu, J. Yu, S. Yan, Saliency Detection by Multitask Sparsity Pursuit, *IEEE Transactions on Image Processing*. 21 (2012) 1327–1338. doi:10.1109/TIP.2011.2169274.
- [97] N. Acito, M. Diani, G. Corsini, Subspace-Based Striping Noise Reduction in Hyperspectral Images, *IEEE Transactions on Geoscience and Remote Sensing*. 49 (2011) 1325–1342. doi:10.1109/TGRS.2010.2081370.
- [98] S.A. Macenka, M.P. Chriss, Airborne Visible/Infrared Imaging Spectrometer (Aviris) Spectrometer Design And Performance, in: *Imaging Spectroscopy II*, International Society for Optics and Photonics, 1987: pp. 32–43. doi:10.1117/12.942281.
- [99] M.L. Eastwood, C.M. Sarture, T.G. Chrien, R.O. Green, W.M. Porter, Current instrument status of the airborne visible/infrared imaging spectrometer (AVIRIS), in: *Infrared Technology XVII*, International Society for Optics and Photonics, 1991: pp. 164–175. doi:10.1117/12.48727.
- [100] S.K. Babey, C.D. Anger, Compact airborne spectrographic imager (CASI): a progress review, in: *Imaging Spectrometry of the Terrestrial Environment*, International Society for Optics and Photonics, 1993: pp. 152–163. doi:10.1117/12.157052.
- [101] Q. Xu, S. Liu, F. Ye, Z. Zhang, C. Zhang, Application of CASI/SASI and fieldspec4 hyperspectral data in exploration of the Baiyanghe uranium deposit, Hebkuesaier, Xinjiang, NW China, *International Journal of Remote Sensing*. 39 (2018) 453–469. doi:10.1080/01431161.2017.1387307.
- [102] G. Jia, A. Hueni, M.E. Schaepman, H. Zhao, Detection and Correction of Spectral Shift Effects for the Airborne Prism Experiment, *IEEE Transactions on Geoscience and Remote Sensing*. 55 (2017) 6666–6679. doi:10.1109/TGRS.2017.2731399.
- [103] F. Kruse, J. Boardman, A. B Lefkoff, J. M Young, K. S Kerein-Young, T. D Cocks, R. Jenssen, P. A Cocks, HyMap: An Australian hyperspectral sensor solving global problems - Results from USA HyMap data acquisitions, in: *Proceedings of the 10th Australasian Remote Sensing and Photogrammetry Conference*, 2000: pp. 18–23.
- [104] D. Schläpfer, R. Richter, Geo-atmospheric processing of airborne imaging spectrometry data. Part 1: Parametric orthorectification, *International Journal of Remote Sensing*. 23 (2002) 2609–2630. doi:10.1080/01431160110115825.
- [105] A. Brunn, C. Fischer, C. Dittmann, R. Richter, Quality Assessment, Atmospheric and Geometric Correction of Airborne Hyperspectral HyMap Data, in: *Proceedings of the 3rd EARSeL Workshop on Imaging Spectroscopy*, 2003: pp. 72–81.
- [106] Z. Malenovský, L. Homolová, R. Zurita-Milla, P. Lukeš, V. Kaplan, J. Hanuš, J.-P. Gastellu-Etchegorry, M.E. Schaepman, Retrieval of spruce leaf chlorophyll content from airborne image data using continuum removal and radiative transfer, *Remote Sensing of Environment*. 131 (2013) 85–102. doi:10.1016/j.rse.2012.12.015.
- [107] J. Hanuš, T. Fabián, L. Fajmon, Potential of Airborne Imaging Spectroscopy at Czechglobe, *ISPRS - International Archives of the Photogrammetry, Remote Sensing and Spatial Information Sciences*. 41B1 (2016) 15–17. doi:10.5194/isprs-archives-XLI-B1-15-2016.
- [108] P. Gege, J. Fries, P. Haschberger, P. Schötz, H. Schwarzer, P. Strobl, B. Suhr, G. Ulbrich, W. Jan Vreeeling, Calibration facility for airborne imaging spectrometers, *ISPRS Journal of Photogrammetry and Remote Sensing*. 64 (2009) 387–397. doi:10.1016/j.isprsjprs.2009.01.006.
- [109] A. Hueni, J. Biesemans, K. Meuleman, F. Dell'Endice, D. Schlapfer, D. Odermatt, M.

- Kneubuehler, S. Adriaensen, S. Kempenaers, J. Nieke, K.I. Itten, Structure, Components, and Interfaces of the Airborne Prism Experiment (APEX) Processing and Archiving Facility, *IEEE Transactions on Geoscience and Remote Sensing.* 47 (2009) 29–43. doi:10.1109/TGRS.2008.2005828.
- [110] B. Gao, M.J. Montes, C.O. Davis, A.F.H. Goetz, Atmospheric correction algorithms for hyperspectral remote sensing data of land and ocean, *Remote Sensing of Environment.* 113 (2009) S17–S24. doi:10.1016/j.rse.2007.12.015.
- [111] A. Ibrahim, B. Franz, Z. Ahmad, R. Healy, K. Knobelspiesse, B.-C. Gao, C. Proctor, P.-W. Zhai, Atmospheric correction for hyperspectral ocean color retrieval with application to the Hyperspectral Imager for the Coastal Ocean (HICO), *Remote Sensing of Environment.* 204 (2018) 60–75. doi:10.1016/j.rse.2017.10.041.
- [112] A. Asmat, E.J. Milton, P.M. Atkinson, Empirical correction of multiple flightline hyperspectral aerial image mosaics, *Remote Sensing of Environment.* 115 (2011) 2664–2673. doi:10.1016/j.rse.2011.05.022.
- [113] R. Marion, R. Michel, C. Faye, Atmospheric correction of hyperspectral data over dark surfaces via simulated annealing, *IEEE Transactions on Geoscience and Remote Sensing.* 44 (2006) 1566–1574. doi:10.1109/TGRS.2006.870408.
- [114] Minu S, Amba Shetty, Atmospheric Correction Algorithms for Hyperspectral Imageries: A Review, *International Research Journal of Earth Sciences.* 3 (2015) 14–18.
- [115] B.D. Bue, D.R. Thompson, M. Eastwood, R.O. Green, B. Gao, D. Keymeulen, C.M. Sarture, A.S. Mazer, H.H. Luong, Real-Time Atmospheric Correction of AVIRIS-NG Imagery, *IEEE Transactions on Geoscience and Remote Sensing.* 53 (2015) 6419–6428. doi:10.1109/TGRS.2015.2439215.
- [116] S. Minu, A. Shetty, B. Gopal, Review of preprocessing techniques used in soil property prediction from hyperspectral data, *Cogent Geoscience.* 2 (2016) 1145878. doi:10.1080/23312041.2016.1145878.
- [117] Q. Cheng, D. Pan, Z. Mao, Atmospheric correction of AISA based on MODTRAN4, in: *Geoinformatics 2006: Remotely Sensed Data and Information,* International Society for Optics and Photonics, 2006: p. 64191Y. doi:10.1117/12.713384.
- [118] A. Rodger, SODA: A new method of in-scene atmospheric water vapor estimation and post-flight spectral recalibration for hyperspectral sensors: Application to the HyMap sensor at two locations, *Remote Sensing of Environment.* 115 (2011) 536–547. doi:10.1016/j.rse.2010.09.022.
- [119] J.E. Conel, R.O. Green, R.E. Alley, C.J. Bruezte, V. Carrere, J.S. Margolis, G. Vane, T.G. Chrien, P.N. Slater, S.F. Biggar, In-Flight Radiometric Calibration Of The Airborne Visible/Infrared Imaging Spectrometer (AVIRIS), in: *Recent Advances in Sensors, Radiometry, and Data Processing for Remote Sensing,* International Society for Optics and Photonics, 1988: pp. 179–195. doi:10.1117/12.945685.
- [120] H. Yang, L. Zhang, C. Ong, A. Rodger, J. Liu, X. Sun, H. Zhang, X. Jian, Q. Tong, Improved Aerosol Optical Thickness, Columnar Water Vapor, and Surface Reflectance Retrieval from Combined CASI and SASI Airborne Hyperspectral Sensors, *Remote Sensing.* 9 (2017) 217. doi:10.3390/rs9030217.
- [121] R. Pelta, E. BenDor, An Exploratory Study on the Effect of Petroleum Hydrocarbon on Soils Using Hyperspectral Longwave Infrared Imagery, *Remote Sensing.* 11 (2019) 569. doi:10.3390/rs11050569.

- [122] R. Beck, S. Zhan, H. Liu, S. Tong, B. Yang, M. Xu, Z. Ye, Y. Huang, S. Shu, Q. Wu, S. Wang, K. Berling, A. Murray, E. Emery, M. Reif, J. Harwood, J. Young, C. Nietch, D. Macke, M. Martin, G. Stillings, R. Stump, H. Su, Comparison of satellite reflectance algorithms for estimating chlorophyll-a in a temperate reservoir using coincident hyperspectral aircraft imagery and dense coincident surface observations, *Remote Sensing of Environment.* 178 (2016) 15–30. doi:10.1016/j.rse.2016.03.002.
- [123] L. Liang, L. Di, L. Zhang, M. Deng, Z. Qin, S. Zhao, H. Lin, Estimation of crop LAI using hyperspectral vegetation indices and a hybrid inversion method, *Remote Sensing of Environment.* 165 (2015) 123–134. doi:10.1016/j.rse.2015.04.032.
- [124] L. Guo, T. Shi, M. Linderman, Y. Chen, H. Zhang, P. Fu, Exploring the Influence of Spatial Resolution on the Digital Mapping of Soil Organic Carbon by Airborne Hyperspectral VNIR Imaging, *Remote Sensing.* 11 (2019) 1032. doi:10.3390/rs11091032.
- [125] Y. Peng, M. Fan, L. Bai, W. Sang, J. Feng, Z. Zhao, Z. Tao, Identification of the Best Hyperspectral Indices in Estimating Plant Species Richness in Sandy Grasslands, *Remote Sensing.* 11 (2019) 588. doi:10.3390/rs11050588.
- [126] C.-C. Liu, T. Hsu, H. Wen, K. Wang, Mapping Pure Mangrove Patches in Small Corridors and Sandbanks Using Airborne Hyperspectral Imagery, *Remote Sensing.* 11 (2019) 592. doi:10.3390/rs11050592.
- [127] F. Chen, K. Wang, T. Van de Voorde, T.F. Tang, Mapping urban land cover from high spatial resolution hyperspectral data: An approach based on simultaneously unmixing similar pixels with jointly sparse spectral mixture analysis, *Remote Sensing of Environment.* 196 (2017) 324–342. doi:10.1016/j.rse.2017.05.014.
- [128] W. Ouerghemmi, C. Gomez, S. Naceur, P. Lagacherie, Semi-blind source separation for the estimation of the clay content over semi-vegetated areas using VNIR/SWIR hyperspectral airborne data, *Remote Sensing of Environment.* 181 (2016) 251–263. doi:10.1016/j.rse.2016.04.013.
- [129] R. Duren, A. Thorpe, S. Sander, California baseline methane survey: Interim phase 1 report, (n.d.). https://ww3.arb.ca.gov/research/methane/ca_ch4_survey_phase1_report_2017.pdf (accessed September 8, 2019).
- [130] A.K. Thorpe, C. Frankenberg, A.D. Aubrey, D.A. Roberts, A.A. Nottrott, T.A. Rahn, J.A. Sauer, M.K. Dubey, K.R. Costigan, C. Arata, A.M. Steffke, S. Hills, C. Haselwimmer, D. Charlesworth, C.C. Funk, R.O. Green, S.R. Lundein, J.W. Boardman, M.L. Eastwood, C.M. Sarture, S.H. Nolte, I.B. McCubbin, D.R. Thompson, J.P. McFadden, Mapping methane concentrations from a controlled release experiment using the next generation airborne visible/infrared imaging spectrometer (AVIRIS-NG), *Remote Sensing of Environment.* 179 (2016) 104–115. doi:10.1016/j.rse.2016.03.032.
- [131] A.K. Ayasse, A.K. Thorpe, D.A. Roberts, C.C. Funk, P.E. Dennison, C. Frankenberg, A. Steffke, A.D. Aubrey, Evaluating the effects of surface properties on methane retrievals using a synthetic airborne visible/infrared imaging spectrometer next generation (AVIRIS-NG) image, *Remote Sensing of Environment.* 215 (2018) 386–397. doi:10.1016/j.rse.2018.06.018.
- [132] I.C. Montero S., G.H. Brimhall, C.N. Alpers, G.A. Swayze, Characterization of waste rock associated with acid drainage at the Penn Mine, California, by ground-based visible to short-wave infrared reflectance spectroscopy assisted by digital mapping, *Chemical Geology.* 215 (2005) 453–472. doi:10.1016/j.chemgeo.2004.06.045.
- [133] N. Richter, T. Jarmer, S. Chabriat, C. Oyonarte, P. Hostert, H. Kaufmann, Free Iron Oxide

- Determination in Mediterranean Soils using Diffuse Reflectance Spectroscopy, *Soil Science Society of America Journal.* 73 (2009) 72–81. doi:10.2136/sssaj2008.0025.
- [134] G.R. Hunt, Spectral signatures of particulate minerals in the visible and near infrared, *GEOPHYSICS.* 42 (1977) 501–513. doi:10.1190/1.1440721.
- [135] V. Kopačková, Using multiple spectral feature analysis for quantitative pH mapping in a mining environment, *International Journal of Applied Earth Observation and Geoinformation.* 28 (2014) 28–42. doi:10.1016/j.jag.2013.10.008.
- [136] L.K. Sørensen, S. Dalsgaard, Determination of Clay and Other Soil Properties by Near Infrared Spectroscopy, *Soil Science Society of America Journal.* 69 (2005) 159–167. doi:10.2136/sssaj2005.0159.
- [137] A. Gobrecht, J.-M. Roger, V. Bellon-Maurel, Chapter Four - Major Issues of Diffuse Reflectance NIR Spectroscopy in the Specific Context of Soil Carbon Content Estimation: A Review, in: D.L. Sparks (Ed.), *Advances in Agronomy*, Academic Press, 2014: pp. 145–175. doi:10.1016/B978-0-12-420225-2.00004-2.
- [138] R.N. Clark, T.V.V. King, M. Klejwa, G.A. Swarze, N. Vergo, High spectral resolution reflectance spectroscopy of minerals, *Journal of Geophysical Research: Solid Earth.* 95 (1990) 12653–12680. doi:10.1029/JB095iB08p12653.
- [139] V. Kopačková, L. Koucká, Integration of Absorption Feature Information from Visible to Longwave Infrared Spectral Ranges for Mineral Mapping, *Remote Sensing.* 9 (2017) 1006. doi:10.3390/rs9101006.
- [140] R. Lucas, P. Bunting, M. Paterson, L. Chisholm, Classification of Australian forest communities using aerial photography, CASI and HyMap data, *Remote Sensing of Environment.* 112 (2008) 2088–2103. doi:10.1016/j.rse.2007.10.011.
- [141] T.J. Arnau, F. Pla, J.M. Sotoca, Vegetation cover estimation from CASI and AHS image sensors, in: *Image and Signal Processing for Remote Sensing XVI*, International Society for Optics and Photonics, 2010: p. 78301M. doi:10.1117/12.865477.
- [142] I.A. Leiper, S.R. Phinn, C.M. Roelfsema, K.E. Joyce, A.G. Dekker, Mapping Coral Reef Benthos, Substrates, and Bathymetry, Using Compact Airborne Spectrographic Imager (CASI) Data, *Remote Sensing.* 6 (2014) 6423–6445. doi:10.3390/rs6076423.
- [143] W. Pan, X. Yang, X. Chen, P. Feng, Application of HyMap image in the environmental survey in Shenzhen, China, in: *Remote Sensing Technologies and Applications in Urban Environments II*, International Society for Optics and Photonics, 2017: p. 104310R. doi:10.1117/12.2278161.
- [144] I. Makki, R. Younes, C. Francis, T. Bianchi, M. Zucchetti, A survey of landmine detection using hyperspectral imaging, *ISPRS Journal of Photogrammetry and Remote Sensing.* 124 (2017) 40–53. doi:10.1016/j.isprsjprs.2016.12.009.
- [145] K.C. Tiwari, M.K. Arora, D. Singh, An assessment of independent component analysis for detection of military targets from hyperspectral images, *International Journal of Applied Earth Observation and Geoinformation.* 13 (2011) 730–740. doi:10.1016/j.jag.2011.03.007.
- [146] H. Chen, X. Du, Z. Liu, Optical spectrum encryption in associated fractional Fourier transform and gyrator transform domain, *Opt Quant Electron.* 48 (2015) 12. doi:10.1007/s11082-015-0291-2.
- [147] S. Tan, Developments in Hyperspectral Sensing, in: J.N. Pelton, S. Madry, S. Camacho-Lara (Eds.), *Handbook of Satellite Applications*, Springer International Publishing, Cham, 2017: pp. 1137–1157. doi:10.1007/978-3-319-23386-4_101.

- [148] H. Chen, Y. Zhang, J. Zhang, Y. Chen, A BOI-Preserving-Based Compression Method for Hyperspectral Images, *IEEE Transactions on Geoscience and Remote Sensing*. 48 (2010) 3913–3923. doi:10.1109/TGRS.2010.2070511.
- [149] P.C. Pandey, N.J. Tate, H. Balzter, Mapping Tree Species in Coastal Portugal Using Statistically Segmented Principal Component Analysis and Other Methods, *IEEE Sensors Journal*. 14 (2014) 4434–4441. doi:10.1109/JSEN.2014.2335612.
- [150] L. Guanter, V. Estellés, J. Moreno, Spectral calibration and atmospheric correction of ultra-fine spectral and spatial resolution remote sensing data. Application to CASI-1500 data, *Remote Sensing of Environment*. 109 (2007) 54–65. doi:10.1016/j.rse.2006.12.005.

Highlights

- 1 This paper depicts the overview of the key technologies for airborne hyperspectral imagers in the past three decades.
- 2 High throughout imaging mode, high quality spectroscopic subsystem, and high sensitivity detector technology are mainly introduced and data pre-processing procedures are described. Some new applications and variations of applications in recent years are also presented.
- 3 By illustrating the status and prospect of typical airborne hyperspectral imagers, this overview provides the comparison of the employed technologies in previous and undergoing research programs and prospect innovative technology for airborne hyperspectral imaging in the future.
- 4 This compilation on hyperspectral imagers used in airborne missions can be served as an important reference to designers who design the future airborne hyperspectral system and researchers who evaluate the data precision of different airborne hyperspectral sensors.

Acknowledgements

The research is financially supported by National Natural Science Foundation of China (Project No. 61627804) and National Key Research Project of China (Project No. 2017YFB0504203).

Declaration of interests

The authors declare that they have no known competing financial interests or personal relationships that could have appeared to influence the work reported in this paper.

The authors declare the following financial interests/personal relationships which may be considered as potential competing interests:

